© 2010 Young Mo Kang

SEMI-ANALYTIC SIMULATIONS OF MICRORING RESONATORS
WITH SCATTERING ELEMENTS

BY

YOUNG MO KANG

THESIS

Submitted in partial fulfillment of the requirements
for the degree of Master of Science in Electrical and Computer Engineering
in the Graduate College of the
University of Illinois at Urbana-Champaign, 2010

Urbana, Illinois

Adviser:

Assistant Professor Lynford L. Goddard

ABSTRACT

This thesis presents theoretical and numerical simulation results of a microring resonator with a scattering element inserted. The spectral reflection of the scattering element can be engineered to realize wavelength-selective reflection for the integrated microring. In particular, a Fabry-Pérot element can be used to produce reflection spectrum with a comb of peaks, whereas a carefully designed distributed Bragg grating can be inserted to realize single peak reflection at the design wavelength. Furthermore, a grating etalon can be used to obtain an ultra-narrow transmission filter or sharp cut-off mirror. The thesis will present semi-analytical solutions to easily anticipate the resultant reflection from the ring for a given scattering element. The results are presented graphically to facilitate understanding of the effects of various design parameters. The structures are candidates for compact planar wavelength-selective mirrors, filters, and switches for dense photonic integrated circuits.

ACKNOWLEDGMENTS

I am grateful to my adviser, Professor Lynford Goddard, for all his guidance and support. I also thank my parents for providing me an invaluable opportunity to study at the University of Illinois.

TABLE OF CONTENTS

CHAPTER 1

INTRODUCTION

Microring resonators are promising building blocks for a variety of optoelectronic and photonic applications, serving as optical switches, filters, modulators, multiplexers, sensors, amplifiers, laser cavities, and logic gates. Their small size and simple structure enable monolithic integration on a single chip, possibly opening the door toward photonic integrated circuits. There has been active research in different shapes and configurations of microring resonators including racetrack design [1], spiral geometry [2], a notched ring [3], multiple rings cascaded in series [4] or in parallel [5], circular arrays [6], 2D arrays [7], and embedded [8]. Most research on microring structures had primarily focused on transmission characteristics. More recently, several studies on microring-based reflectors have been reported [3, 6, 9, 10, 11, 12, 13, 14, 15]. In this thesis, a single microring structure coupled to a waveguide with a general scattering element inserted in the ring will be analyzed. In particular, periodic-peak reflection, single-peak reflection, ultra-narrow transmission filter, and sharp cut-off mirror configurations of microring structures will be discussed. These ultra-compact microring-based reflectors are candidates for in-plane wavelength-selective mirrors, filters, and switches for various applications, allowing high density integration into planar optoelectronic circuits.

1.1 Current Research in the Field

Most microring-based structures proposed and fabricated by researchers are transmissive wavelength-selective elements, but more recently there have been several reports on reflective microring-based structures. A structure comprising two-rings cascaded to a single bus waveguide (Fig. 1.1a) was investigated [9] where both rings are coupled to the bus waveguide,
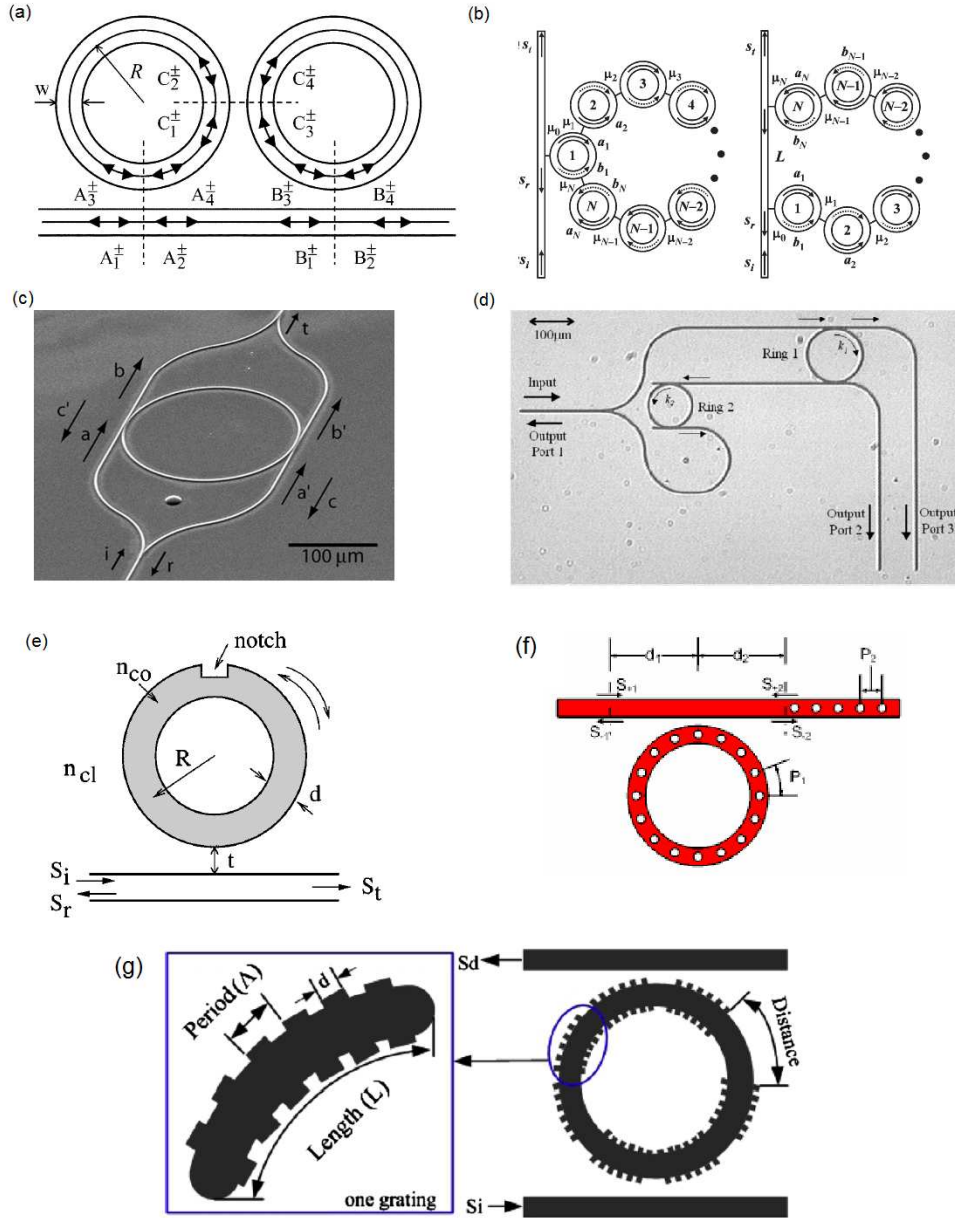
Figure 1.1: Various designs for obtaining counter-propagating fields. (a) Double-ring resonator system coupled to a waveguide [9]. (b) Circular arrays of coupled microring resonators [6]. (c) A microring inserted between two Y-junctions [12]. (d) Cascaded microring add/drop filters coupled to arms of a Y-junction [13]. (e) A single notched microring [3]. (f) A microring with one-dimensional photonic crystal defects [15]. (g) A microring with quasi-grating sidewall corrugation [16].

and at the same time there is direct inter-resonator coupling between the two rings. The structure results in a single- to four-peak reflection profile depending on coupling coefficients involved.

A more complicated version employs a circular array of multiple microring resonators (Fig. 1.1b), coupled to adjacent rings or the bus waveguide [10]. To achieve counter-propagating waves in this architecture, a serial reflection filter topology is used for an array of odd number microrings, where only one microring is coupled to the bus waveguide. For an even number of microrings, a parallel topology is used, where two microrings are each coupled to the bus waveguide. Employing multiple microring resonators in this geometry achieves super-flat bandpass response.

Another research group investigated two major configurations of ring-based inline reflectors employing Y-junctions. In the first structure [12], a straight waveguide is split into two arms by a Y-junction and combined by another opposite-direction Y-junction, resembling the Mach-Zehnder modulator geometry. In the central portion between the Y-junctions, a microring is inserted and coupled to each arm (Fig. 1.1c). In the second design [13], optical input is split into two by a Y-junction, and the signal in each arm is filtered twice by passing through the cascaded microring add/drop filters, exiting back to the input port or to two additional output ports (Fig. 1.1d). In both designs, single- or periodic-peak reflection is possible using different microring radii (Vernier effect).

The simplest design to date was proposed by Little et al. [3]. A small perturbation is introduced to a microring coupled to a bus waveguide by a single notch at the center of the ring (Fig. 1.1e). The structure was analyzed and numerically simulated using finite-difference time-domain (FDTD) method. With a well-designed notch dimension, periodic peaks of maximum reflection were realized, but as the notch size increases, the perturbation increases, and the response exhibits increasing ripple in each peak.

Goldring *et al.* studied a microring reflector with one-dimensional photonic crystal (PhC) bandgaps [15]. In the notch filter configuration, a microring is coupled to a single waveguide, where unity-reflection mirror by one-dimensional PhC defects is placed at the through port as illustrated in Fig. 1.1f. Another set of one-dimensional PhC defects of different period is placed in the ring waveguide in order to increase modal dispersion, which leads to narrowing

3

of the spectral linewidth of the structure. It should be noted that the reflection is achieved from the mirror placed at the through port, and the PhC defects in the ring serve as the mechanism to induce large group index near the photonic bandgap. In a similar fashion, Wang *et al.* studied the effect of quasi-grating sidewall corrugation resulting from fabrication issues of a microring resonator system [16], as depicted in Fig. 1.1g. The reflectivity of the quasi-grating leads to mutual mode coupling between the forward- and backward-propagating modes in the ring, resulting in resonance splitting. It should be noted, however, that its reflection spectrum was not studied in the paper.

1.2   Research Motivation and Outline

The notched microring structure is by far the simplest and the most compact structure among the configurations discussed above, which makes it suitable to design, integrate, and fabricate on an optical chip with high density. In order to realize such design flexibility, it is highly desired that more detailed investigation and analysis be carried out on these types of reflecting microring structures employing various elements not limited to a single notch, but to any physically realizable elements that can be incorporated. In other words, one needs to examine a generic case scattering-induced microring mirror. In this paper, a general form system will be first formulated, such that given some scattering element introduced in the ring, the reflection and transmission spectrum of this microring mirror is easily predicted. Using the methods presented here, one can cleverly engineer a wavelength selective response by inserting the appropriate scattering element.

CHAPTER 2

FUNDAMENTALS

In this chapter, I will briefly review some of the theoretical and fundamental background of microring resonators.

2.1 A General Microring Resonator

When two waveguides are adjacent to each other, modes propagating in the waveguides couple to each other by the coupling equation described by

$$\begin{bmatrix} b_1 \\ b_2 \end{bmatrix} = \mathbf{K} \begin{bmatrix} a_1 \\ a_2 \end{bmatrix} \tag{2.1}$$

where a_i, b_i are the complex mode amplitudes[1] of the four-port coupler as illustrated in Fig. 2.1, $\mathbf{K} = \begin{bmatrix} \tau & j\kappa \\ j\kappa & \tau \end{bmatrix}$ is the coupling matrix, and κ and τ are the real-valued coupling and transmission coefficients, respectively [17]. The details and derivations of the coupling equation are not covered in this thesis. For lossless coupling condition, we have

$$\kappa^2 + \tau^2 = 1 \tag{2.2}$$

which will be the condition assumed throughout the thesis unless specified otherwise. We will also assume that $\mathbf{K}$ is spectrally constant, which is a valid approximation in the cases where the coupling interaction length is very small [18, Ch. 3].

We are interested in the steady-state spectral dependence of output power $|b_1|^2$ given a

---

[1]These quantities are normalized in power such that the squares of their amplitudes are proportional to the intensities of the signals. Throughout the thesis, any signal is assumed to be represented in this manner.
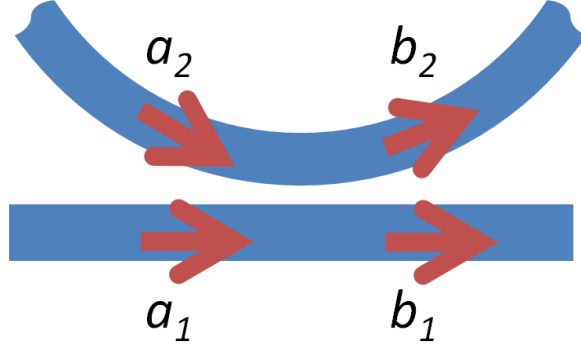
Figure 2.1: Four-port coupler schematic diagram. Signals a_1, b_1 represent the input and transmission signals, respectively.

general relation,

$$a_2 = x b_2 \tag{2.3}$$

where a general propagation term $x = |x|e^{\phi_x}$ describes the amplitude and phase shift per round trip in the ring. The value of x is determined from the geometry and configuration of the microring resonator. For example, $|x| > 1$ implies gain of the signal in the microring. Solving Eq. (2.1) through Eq. (2.3) simultaneously yields

$$a_2 = \frac{j\kappa x}{1 - \tau x} a_1 \tag{2.4}$$

$$|a_2|^2 = \frac{\kappa^2 |x|^2}{1 - 2\tau|x|\cos\phi_x + \tau^2|x|^2} |a_1|^2 \tag{2.5}$$

$$b_1 = \frac{\tau - x}{1 - \tau x} a_1 \tag{2.6}$$

$$|b_1|^2 = \frac{\tau^2 - 2\tau|x|\cos\phi_x + |x|^2}{1 - 2\tau|x|\cos\phi_x + \tau^2|x|^2} |a_1|^2 \tag{2.7}$$

$$= \left(1 - \frac{(1 - \tau^2)(1 - |x|^2)}{1 - 2\tau|x|\cos\phi_x + \tau^2|x|^2} \right) |a_1|^2. \tag{2.8}$$

It is also possible to derive complete analytic time-domain solution of a constant input. Let the input signal turn on at time $t = 0$, i.e., $a_1(t) = 0$ for $t < 0$ and $a_1(t) = a_{1_0}$ for $t \geq 0$. Let t_0 be the time delay for optical signal to travel one round trip in the ring. Note that any change in the input field propagates in multiples of time delay mt_0. Hence, it is sufficient to describe the fields in discrete time-domain mt_0, m is an integer, rather than continuous

time-domain t.

Let sequences a_{i_m} and b_{i_m} describe the fields during time $mt_0 \leq t < (m+1)t_0$. We first note that

$$a_{1_m} = \begin{cases} 0 & \text{for } m < 0, \\ a_{1_0} & \text{for } m \geq 0. \end{cases} \tag{2.9}$$

In addition, we define initial conditions

$$a_{2_m} = b_{1_m} = b_{2_m} = 0 \qquad \text{for } m < 0. \tag{2.10}$$

Equation (2.1) is re-written as

$$\begin{bmatrix} b_{1_m} \\ b_{2_m} \end{bmatrix} = \mathbf{K} \begin{bmatrix} a_{1_m} \\ a_{2_m} \end{bmatrix}, \tag{2.11}$$

and Eq. (2.3) is re-written as

$$a_{2_{m+1}} = x b_{2_m}. \tag{2.12}$$

Solving Eq. (2.9) through Eq. (2.12) yields

$$b_{2_m} = j\kappa a_{1_0} + \tau x b_{2_{m-1}} \qquad \text{for } m \geq 0. \tag{2.13}$$

The solution to the sequence Eq. (2.13) is given by

$$b_{2_m} = j\kappa a_{1_0} \sum_{i=0}^{m} (\tau x)^m \qquad \text{for } m \geq 0 \tag{2.14}$$

$$= j\kappa \frac{1 - (\tau x)^m}{1 - \tau x} a_{1_0} \qquad \text{for } m \geq 0. \tag{2.15}$$

Substituting Eq. (2.15) into Eq. (2.11) yields

$$b_{1_m} = \begin{cases} \tau a_{1_0} & \text{for } m = 0, \\ \frac{\kappa^2 x (\tau x)^{m-1} + \tau - x}{1 - \tau x} a_{1_0} & \text{for } m \geq 1. \end{cases} \tag{2.16}$$

Note that the result in Fig. 2.2 agrees with Eq. (2.6) for $m = \infty$ when $|\tau x| < 1$. The
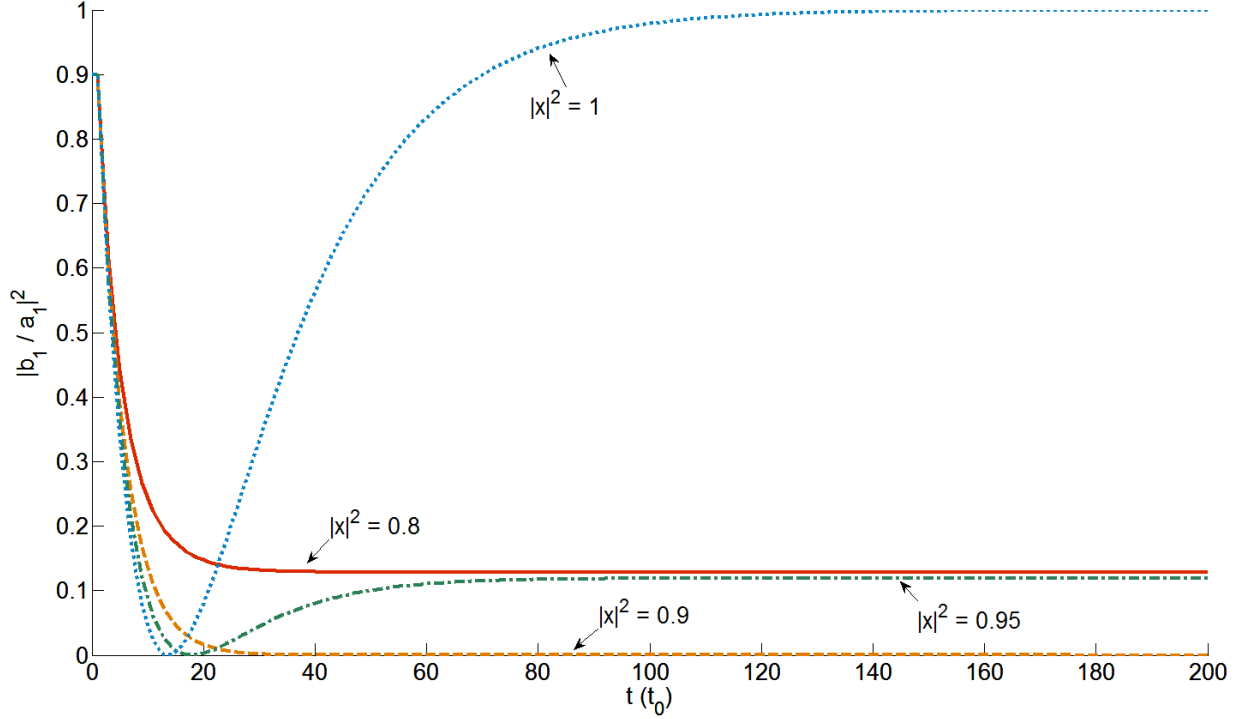
7

Figure 2.2: Time-domain response of the output to a step input for various values of $|x|^2$ for $\kappa^2 = 0.1$ at resonance.

figure plots the time-domain response of the output intensity at the resonance wavelength for various values of $|x|^2$ at $\kappa^2 = 0.1$. For $|x|^2 < \kappa^2$, $|x|^2 = \kappa^2$, and $|x|^2 > \kappa^2$, the transient response resembles that of an overdamped, a critically damped, and an underdamped system, respectively.

Figure 2.3 depicts a typical spectral response of the build-up factor $\left|\frac{a_2^2}{a_1^2}\right|$ inside the ring as a function of ϕ_x. The free spectral range (FSR) is the spacing between two successive intensity maxima, and the full width at half maximum (FWHM) is the spacing between the two points at the half of the maximum value near the peak. Finesse F is the ratio of the FSR to the FWHM, and quality factor Q is the ratio of the resonant angular frequency ω_r to the FWHM.
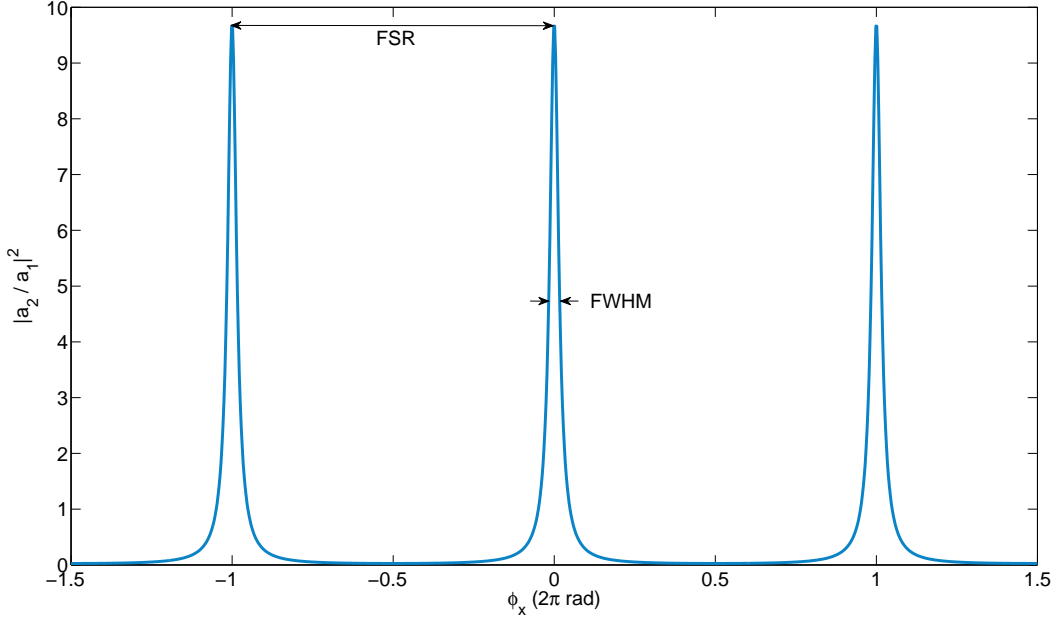
Figure 2.3: Typical build up factor for a resonator.

2.2 A Microring Coupled to Single Waveguide

In this section, an analysis of the plain microring resonator will be presented closely following ref. [18, 19]. Figure 2.4 depicts two configurations used for filtering out specific wavelengths of the input signal. For Fig. 2.4a, we let

$$x = \alpha e^{j\beta L} = \alpha e^{j\theta} \tag{2.17}$$

$$\theta = \beta L \tag{2.18}$$

where real values α and θ are the amplitudes and phase factor per round trip in the ring, respectively. $\beta = kn_e = \frac{2\pi}{\lambda}n_e$ is the modal propagation constant in the ring waveguide where λ is the wavelength in free space,[2] $n_e = \frac{\beta}{k}$ is the effective modal index of the ring, and L is

---

[2]Throughout the thesis, λ denotes the wavelength in free space, and $\lambda_e = \frac{\lambda}{n_e}$ denotes the effective wavelength in the waveguide. The subscript 0 is used to denote the design parameter. For example, β_0 is the modal propagation constant at the design wavelength λ_0.
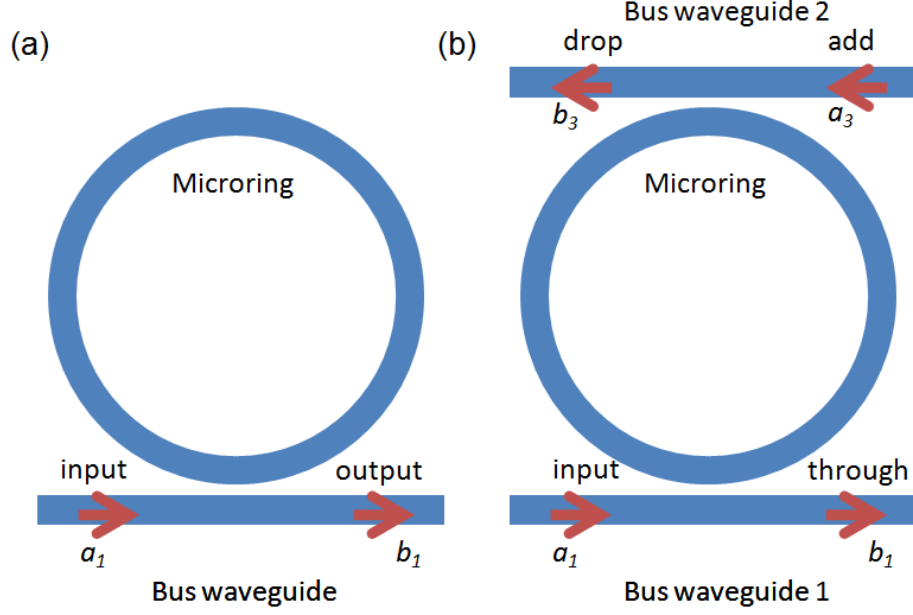
Figure 2.4: (a) A microring coupled to a single waveguide. (b) A microring coupled to two waveguides.

the circumference of the ring. Plugging Eq. (2.17) into Eq. (2.8) yields

$$|b_1|^2 = \left(1 - \frac{(1 - \tau^2)(1 - \alpha^2)}{1 - 2\tau\alpha\cos\theta + \tau^2\alpha^2}\right)|a_1|^2. \tag{2.19}$$

Figure 2.5 plots the output intensity normalized to the input at various $\alpha^2 < 1$ in the ring for fixed $\tau^2 = 1 - \kappa^2 = 0.9$. As α increases, the dips become sharper. From Eq. (2.19) we see that: (1) the maxima occur at $\theta = (2m - 1)\pi$ and (2) minima occur at $\theta = 2m\pi$, m is an integer. For the critical coupling condition $\alpha = \tau$ [19], the minima become null. We also see that for lossless ring, *i.e.*, $\alpha^2 = 1$, the output intensity is always equal to the input intensity, which confirms energy conservation law.

At resonance, $\theta = \frac{2\pi\nu}{c}n_e L = 2m\pi$, and hence the FSR in frequency is given by

$$\nu_{FSR} = \Delta\nu = \frac{c}{n_g L}, \tag{2.20}$$

where

$$n_g = \frac{\partial\beta}{\partial k} = n_e + \omega\frac{\partial n_e}{\partial\omega} = n_e - \lambda\frac{\partial n_e}{\partial\lambda} \tag{2.21}$$
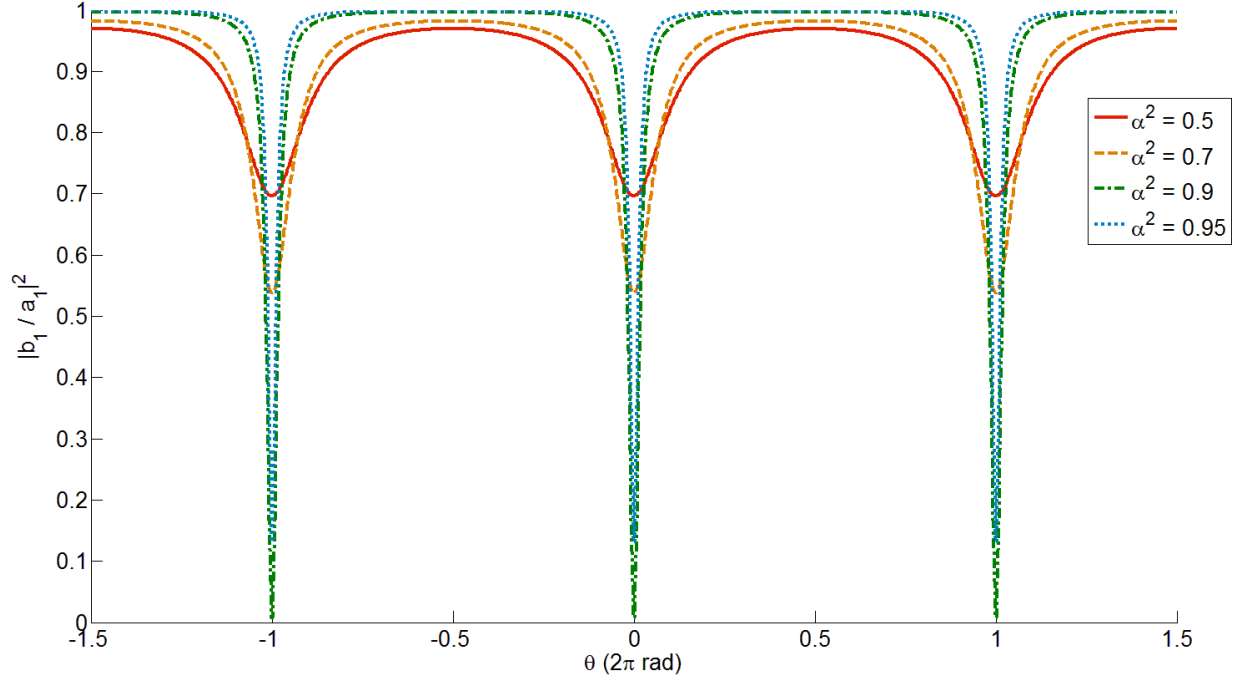
10

Figure 2.5: Through port intensity normalized to input for $\tau^2 = 0.9$.

is the group index. Sometimes it is more convenient to write the FSR in wavelength,

$$\lambda_{FSR} = \Delta\lambda \approx |\frac{\partial\lambda}{\partial\nu}|\Delta\nu = \frac{\lambda^2}{n_g L}. \tag{2.22}$$

Using Eq. (2.5), the FWHM of the field buildup $|\frac{a_2}{a_1}|^2$ is calculated by solving for $\delta\theta$ in the following equation [18, Ch. 3]:

$$\frac{1}{2} \cdot \frac{\alpha^2\kappa^2}{1 - 2\alpha\tau + \alpha^2\tau^2} = \frac{\alpha^2\kappa^2}{1 - 2\alpha\tau\cos\delta\theta + \alpha^2\tau^2}, \tag{2.23}$$

from which we obtain

$$\cos\delta\theta = \frac{-1 + 4\alpha\tau - \alpha^2\tau^2}{2\alpha\tau} \tag{2.24}$$

$$= 1 - \frac{(1-\alpha\tau)^2}{2\alpha\tau}. \tag{2.25}$$

11

For $\alpha\tau \approx 1$, we can use the approximation $\cos\delta\theta \approx 1 - \frac{\delta\theta^2}{2}$ since $\delta\theta \ll 1$:

$$\delta\theta \approx \frac{1-\alpha\tau}{\sqrt{\alpha\tau}} \tag{2.26}$$

$$\nu_{FWHM} = 2\delta\nu = 2 \cdot \frac{c\delta\theta}{2\pi n_g L} \approx \frac{c(1-\alpha\tau)}{\pi n_g L \sqrt{\alpha\tau}}. \tag{2.27}$$

In wavelength, we obtain

$$\lambda_{FWHM} = 2\delta\lambda \approx |\frac{\partial\lambda}{\partial\nu}|2\delta\nu = \frac{\lambda^2(1-\alpha\tau)}{\pi n_g L \sqrt{\alpha\tau}}. \tag{2.28}$$

2.3   A Microring Coupled to Two Waveguides

Figure 2.4b depicts an add/drop filter. Instead of attenuating resonant frequencies by optical loss in the ring, the add/drop configuration filters out resonant frequencies to the drop port. We let

$$x = \alpha\tau e^{j\theta} \tag{2.29}$$

assuming that the coupling coefficients are identical at both waveguides. For a lossless ring, *i.e.*, $\alpha^2 = 1$, we note that from conservation of energy, when there is no signal from the add port, the drop port signal power must equal to the input subtracted by the through port, given by

$$|b_3|^2 = |a_1|^2 - |b_1|^2 = \frac{(1-\tau^2)^2}{1-2\tau^2\cos\theta+\tau^4}|a_1|^2. \tag{2.30}$$

Figure 2.6 plots the through port and drop port intensity of a lossless microring at various values of τ^2. Note that for a lossless ring, the maxima are always unity regardless of the value of τ^2. In general, the larger the value of τ^2, *i.e.*, the smaller the value of κ^2, the narrower the FWHM becomes. In the presence of input at the add port, we can easily obtain the solution by invoking the law of superposition because the system is linear.

For a lossless case, the FSR is identical to Eq. (2.20) and Eq. (2.22), and the FWHM of
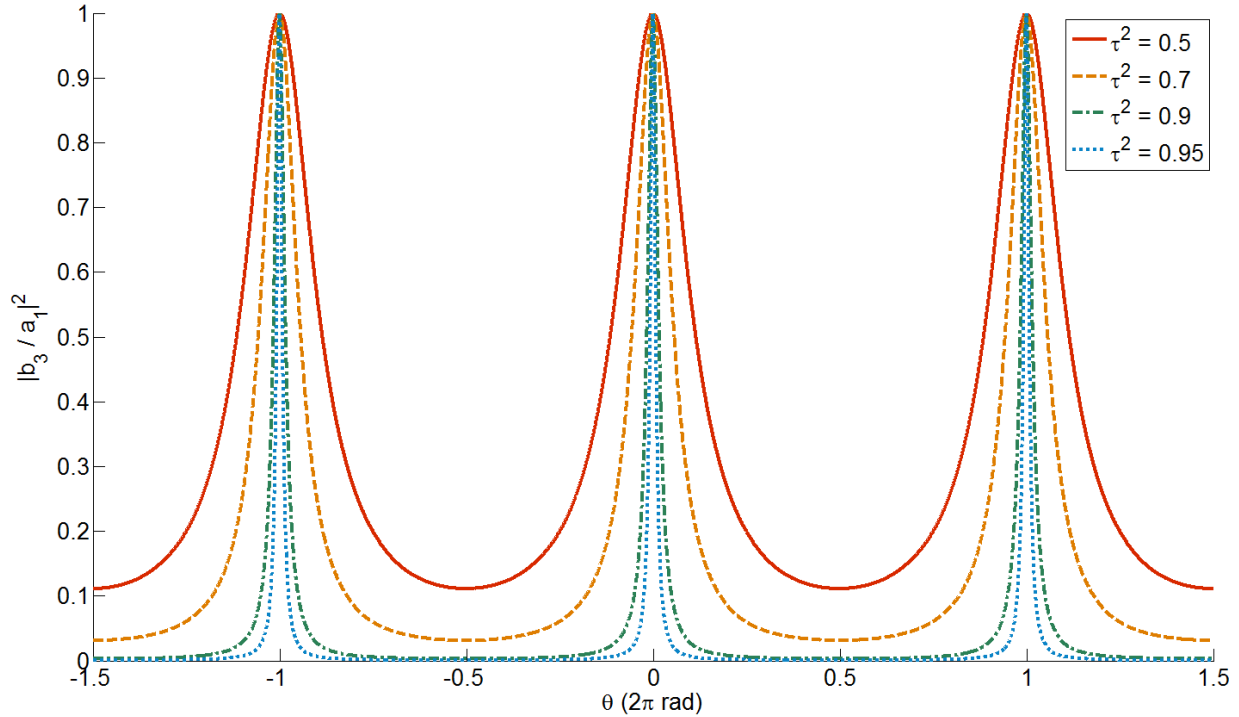
Figure 2.6: Drop port intensity normalized to input.

the drop power $|\frac{b_3}{a_1}|^2$ is given by

$$\nu_{FWHM} = 2\delta\nu \quad \approx \quad \frac{c\kappa^2}{\pi\tau n_g L} \tag{2.31}$$

$$\lambda_{FWHM} = 2\delta\lambda \quad \approx \quad \frac{\lambda^2\kappa^2}{\pi\tau n_g L}. \tag{2.32}$$

2.4 Fabry-Pérot Resonator

The Fabry-Pérot (FP) resonator is another very simple resonator, which consists of two reflective elements as shown in Fig. 2.7. To solve for steady state output intensity $|a_2|^2$, we let the field at the position right after the first mirror M_1 be x. Assuming lossless material inside the resonator and that there is no incident signal from the second mirror M_2, *i.e.*,
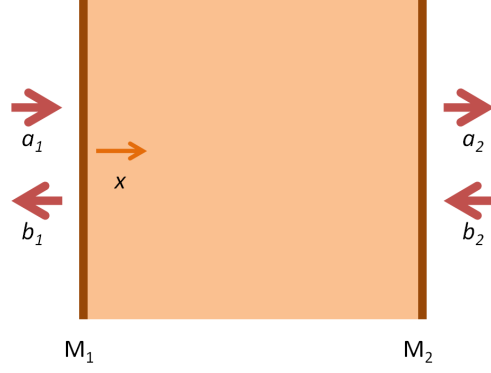
Figure 2.7: Schematic diagram of a Fabry-Pérot resonator consisting of two mirrors.

$b_2 = 0$, we note that x must satisfy the following steady state equation:

$$x = t_{1,R}a_1 + r_{1,L}r_{2,R}xe^{j2\theta_d} \tag{2.33}$$

$$\theta_d = \beta d \tag{2.34}$$

where $r_{m,n}$, $t_{m,n}$, $m = 1, 2$, and $n = L, R$ are normalized reflection and transmission coefficients for the fields moving in each direction at each mirror, respectively, as described in Fig. 2.8 where d is the separation distance of the two mirrors. Solving Eq. (2.33), we obtain

$$x = \frac{t_{1,R}}{1 - r_{1,L}r_{2,R}e^{j2\theta_d}}a_1 \tag{2.35}$$

$$a_2 = t_{2,R}xe^{j\theta_d} = \frac{t_{1,R}t_{2,R}e^{j\theta_d}}{1 - r_{1,L}r_{2,R}e^{j2\theta_d}}a_1 \tag{2.36}$$

$$|a_2|^2 = \frac{t_{1,R}^2 t_{2,R}^2}{1 - 2r_{1,L}r_{2,R}cos2\theta_d + r_{1,L}^2 r_{2,R}^2}|a_1|^2 \tag{2.37}$$

$$b_1 = r_{1,R}a_1 + r_{2,R}t_{1,L}xe^{j2\theta_d} = \frac{r_{1,R} - (r_{1,L}r_{1,R} - t_{1,L}t_{1,R})r_{2,R}e^{j2\theta_d}}{1 - r_{1,L}r_{2,R}e^{j2\theta_d}}a_1^- \tag{2.38}$$

where $r_{m,n}$ and $t_{m,n}$ are assumed to be real. We note that Eq. (2.37) is in equivalent form to Eq. (2.30) in the case where two mirrors are identical, $i.e.$, $r_{1,L} = r_{2,R} = r$, and the mirrors are lossless, $i.e.$, $r_{k,l}^2 + t_{k,l}^2 = 1$, and reciprocal[3], $i.e.$, $t_{k,L} = t_{k,R}$.

A different approach involves decomposition of a given FP resonator into three network

---

[3]Throughout the thesis, I will assume that all optical elements are reciprocal networks for normalized fields. This is valid for any system which satisfy Maxwell's equations with scalar ε and μ [20, Ch. 3].
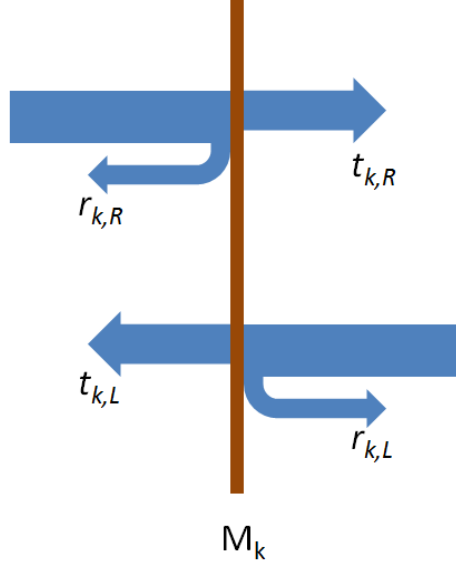
14

Figure 2.8: Reflection and transmission coefficients notations.

systems as shown in Fig. 2.9a. Each network's four ports are related by scattering $\mathbf{S}$ or transmission $\mathbf{T}$ matrices [20, Ch. 3] as follows:

$$\begin{bmatrix} y_1 \\ x_2 \end{bmatrix} = \mathbf{S} \begin{bmatrix} x_1 \\ y_2 \end{bmatrix} = \begin{bmatrix} S_{11} & S_{12} \\ S_{21} & S_{22} \end{bmatrix} \begin{bmatrix} x_1 \\ y_2 \end{bmatrix} \tag{2.39}$$

$$\begin{bmatrix} x_1 \\ y_1 \end{bmatrix} = \mathbf{T} \begin{bmatrix} x_2 \\ y_2 \end{bmatrix} = \begin{bmatrix} T_{11} & T_{12} \\ T_{21} & T_{22} \end{bmatrix} \begin{bmatrix} x_2 \\ y_2 \end{bmatrix} \tag{2.40}$$

where x_i and y_i are signals at the four ports as described in Fig. 2.9b. The scattering and transmission matrices themselves are related by

$$\mathbf{S} = \frac{1}{T_{11}} \begin{bmatrix} T_{21} & \det \mathbf{T} \\ 1 & -T_{12} \end{bmatrix} \tag{2.41}$$

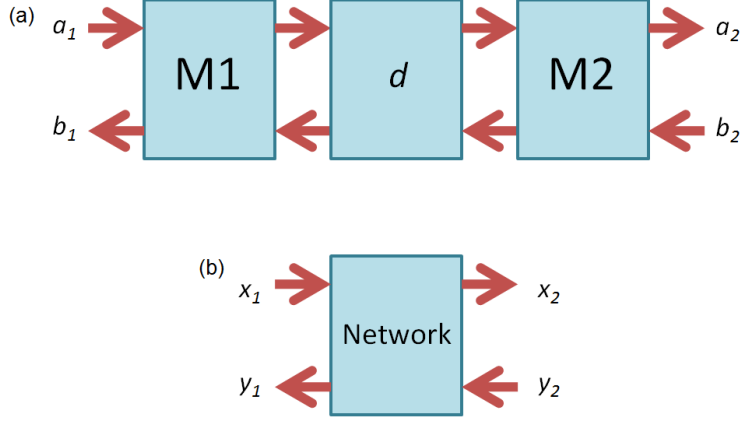$$\mathbf{T} = \frac{1}{S_{21}} \begin{bmatrix} 1 & -S_{22} \\ S_{11} & -\det \mathbf{S} \end{bmatrix}. \tag{2.42}$$

Figure 2.9: (a) A FP resonator decomposed into three networks: two mirrors M_1 and M_2, and a propagation distance d. (b) A four-port network schematic diagram.

For a mirror network M_k, we readily see that

$$\mathbf{S_{M_k}} = \begin{bmatrix} r_{k,R} & t_{k,L} \\ t_{k,R} & r_{k,L} \end{bmatrix} \tag{2.43}$$

from Fig. 2.8. For a propagation network of distance d, we can easily verify

$$\mathbf{S_d} = \begin{bmatrix} 0 & e^{j\theta_d} \\ e^{j\theta_d} & 0 \end{bmatrix}. \tag{2.44}$$

Converting Eq. (2.43) and Eq. (2.44) into transmission matrices using Eq. (2.42) and multiplying them out yields the transmission matrix of the FP resonator,

$$\mathbf{T} = \mathbf{T_{M_1} T_d T_{M_2}} \tag{2.45}$$

where we note that matrix multiplication of transmission matrices solves the system of the cascaded networks. Finally, the transmitted signal a_2 in the absence of b_2 of the FP resonator can then be solved from

$$a_2 = S_{21} a_1 = \frac{1}{T_{11}} a_1, \tag{2.46}$$

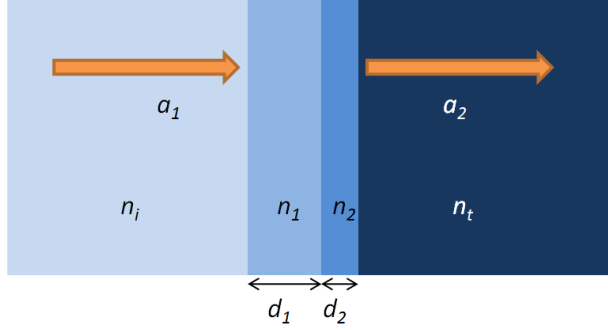which agrees with Eq. (2.36). In a similar fashion, the reflected field b_1 can also be found

Figure 2.10: A multi-layered system of different refractive indices.

from

$$b_1 = S_{11}a_1 = \frac{T_{21}}{T_{11}}a_1. \tag{2.47}$$

2.5 Multi-Layered System

The transmission matrix method can be used to numerically evaluate an arbitrary multi-layered system of different refractive indices. Consider a system consisting of four layers as shown in Fig. 2.10. The input signal a_1 in a medium with modal index n_i is incident on two layers of indices n_1 and n_2, and we are interested in the output signal a_2 transmitted to medium of index n_t. There are three mirror interfaces: $(n_L, n_R) = (n_i, n_1)$, (n_1, n_2), and (n_2, n_t). If we assume for simplicity that the material refractive index is identical to the modal index, we obtain the scattering matrix for each mirror,

$$\mathbf{S} = \begin{bmatrix} \frac{n_L - n_R}{n_L + n_R} & \frac{2n_L}{n_L + n_R}\sqrt{\frac{n_R}{n_L}} \\ \frac{2n_R}{n_L + n_R}\sqrt{\frac{n_L}{n_R}} & \frac{n_R - n_L}{n_L + n_R} \end{bmatrix} = \begin{bmatrix} r & t \\ t & -r \end{bmatrix}. \tag{2.48}$$

The rest is very similar to the method described in Section 2.4. This method can be extended to any number of arbitrary layers. In particular, the numerical simulation of a Bragg grating's reflectance spectrum, which will be discussed in the next chapter, can be evaluated from this transfer matrix approach.

17

CHAPTER 3

MICRORING WITH REFLECTIVE ELEMENT

This chapter presents analysis and numerical simulations of microring resonators integrated with various reflective elements.

3.1   General Analysis

We extend the previous simple model of a general microring resonator analysis presented in Section 2.1 to account for reflection occurring in the microring. In particular, we model a reflective element as a four-port network, and we let $\mathbf{S} = \begin{bmatrix} S_{11} & S_{12} \\ S_{21} & S_{22} \end{bmatrix}$ be the scattering matrix of the network, as depicted in Fig. 3.1. Due to the reflection at the network, there will be fields propagating in both counterclockwise and clockwise directions in the microring, and hence we use superscripts $+$ and $-$ to indicate the fields propagating in these directions, respectively. I will closely follow the analysis presented in [21, 22]. Assuming a symmetric coupling between the microring and the waveguide, we have two sets of coupling equations

$$\begin{bmatrix} b_1^+ \\ b_2^+ \end{bmatrix} = \mathbf{K} \begin{bmatrix} a_1^+ \\ a_2^+ \end{bmatrix} \tag{3.1}$$

$$\begin{bmatrix} a_1^- \\ a_2^- \end{bmatrix} = \mathbf{K} \begin{bmatrix} b_2^- \\ b_2^- \end{bmatrix}, \tag{3.2}$$

which are equivalent to Eq. (2.1). For simplicity, we assume that the reflective element is introduced at the upper center of the ring, such that there is equal distance $\frac{L}{2}$ for both $+$ and $-$ waves to reach the element from the coupling region. Again, let Eq. (2.17) describe the amplitude and phase change per round trip in the ring in the absence of the reflective
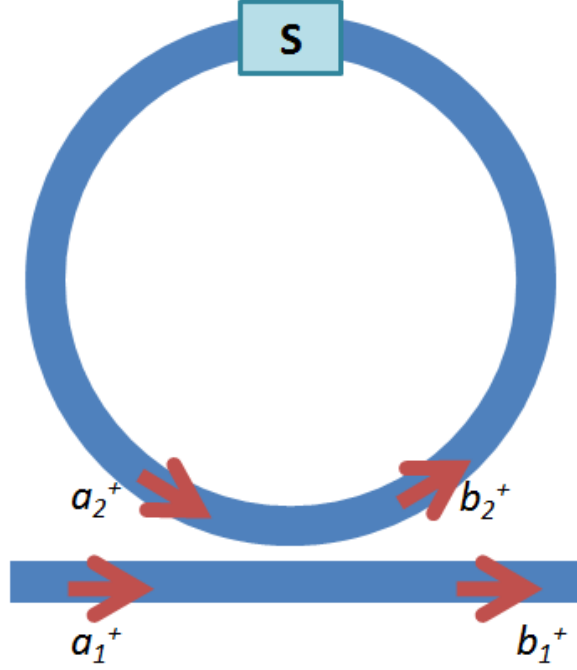
Figure 3.1: A schematic diagram of a microring resonator with a reflective element.

element. Combining Eq. (2.17) and Eq. (2.39), we obtain

$$
\begin{bmatrix} a_2^+ \\ b_2^- \end{bmatrix} = \alpha e^{j\theta} \mathbf{S} \begin{bmatrix} a_2^- \\ b_2^+ \end{bmatrix}.
\tag{3.3}
$$

Solving Eq. (3.1) through Eq. (3.3) for $b_1^- = 0$ yields

$$
b_1^+ = \frac{\tau - \alpha \left(S_{12}\kappa^2 + (S_{12} + S_{21})\,\tau^2 \right) e^{j\theta} - \alpha^2 \tau e^{j2\theta} \det \mathbf{S}}{1 - \alpha \left(S_{12} + S_{21} \right) \tau e^{j\theta} - \alpha^2 \tau^2 e^{j2\theta} \det \mathbf{S}} a_1^+
\tag{3.4}
$$

$$
a_1^- = \frac{-\alpha S_{22}\kappa^2 e^{j\theta}}{1 - \alpha \left(S_{12} + S_{21} \right) \tau e^{j\theta} - \alpha^2 \tau^2 e^{j2\theta} \det \mathbf{S}} a_1^+,
\tag{3.5}
$$

where b_1^+ and a_1^- are transmitted and reflected field of the general reflective microring structure, respectively.

3.2 Graphical Solutions

For simplicity, we assume that the network is lossless reciprocal,[1] and $a_1^+ = 1$. Substituting Eq. (A.21) into Eq. (3.4) and Eq. (3.5) yields

$$b_1^+ = \frac{\tau - \alpha|t|\left(1+\tau^2\right)e^{j\left(\theta+\psi+\frac{\pi}{2}\right)} + \alpha^2\tau e^{j2\left(\theta+\psi+\frac{\pi}{2}\right)}}{1 - 2\alpha|t|\tau e^{j\left(\theta+\psi+\frac{\pi}{2}\right)} + \alpha^2\tau^2 e^{j2\left(\theta+\psi+\frac{\pi}{2}\right)}} \tag{3.6}$$

$$a_1^- = \frac{j\alpha r^*\left(1-\tau^2\right)e^{j\left(\theta+\psi+\frac{\pi}{2}\right)}}{1 - 2\alpha|t|\tau e^{j\left(\theta+\psi+\frac{\pi}{2}\right)} + \alpha^2\tau^2 e^{j2\left(\theta+\psi+\frac{\pi}{2}\right)}}, \tag{3.7}$$

where $\theta = \beta L$ is the round-trip phase change in the ring, and $\theta_s = \psi + \frac{\pi}{2}$ is the transmission phase change in the scattering element. Note that $S_{12} = j|t|e^{j\psi}$ is the transmission coefficient of the scattering element, and therefore $\psi + \frac{\pi}{2}$ represents the transmission phase shift due to the element.

Let us assume that we have analytic or numerical values of $\tau(\beta)$, $\alpha(\beta)$, and $\theta(\beta)$. We can then plot a contour graph of $|a_1^-|^2$ as a function of total detuned phase shift $\Theta = \theta + \theta_s - \beta_0 L_t$ and magnitude of reflection from the element $|r| = \sqrt{1-|t|^2}$ on the Θ - $|r|$ plane. Here, $L_t = L + d$ is the total circumference of the integrated microring structure[2] where L is the ring-only circumference and d is the length of the inserted scattering element. Similarly, if the inserted network's reflectivity $|re^{j\psi}|$ as a function of β is already known, we can overlay its spectral reflectivity graph on the same Θ - $|r|$ plane. By examining the two graphs on the same plane, we can visualize the effect of the inserted network on the reflected field intensity of the integrated microring resonator.

The colored part of Fig. 3.2 is the contour graph of $|a_1^-|^2$ for $\alpha^2 = 1$ and $\kappa^2 = 0.1$, which are assumed to be constants over β. We can see that at $|r| \approx 0.05$, the reflection from the integrated microring becomes unity at the resonance condition $\Theta = 2m\pi$. If we increase the reflectivity of the inserted network, we observe that the peak reflection of the ring starts to split into two. This is the resonance-splitting caused by mutual coupling between the forward and backward modes in the ring [16, 23].

---

[1]Refer to Section A.4 for details.

[2]Throughout the thesis, L_t will be assumed to be an integer multiple of the effective design wavelength $\lambda_{0,e}$.
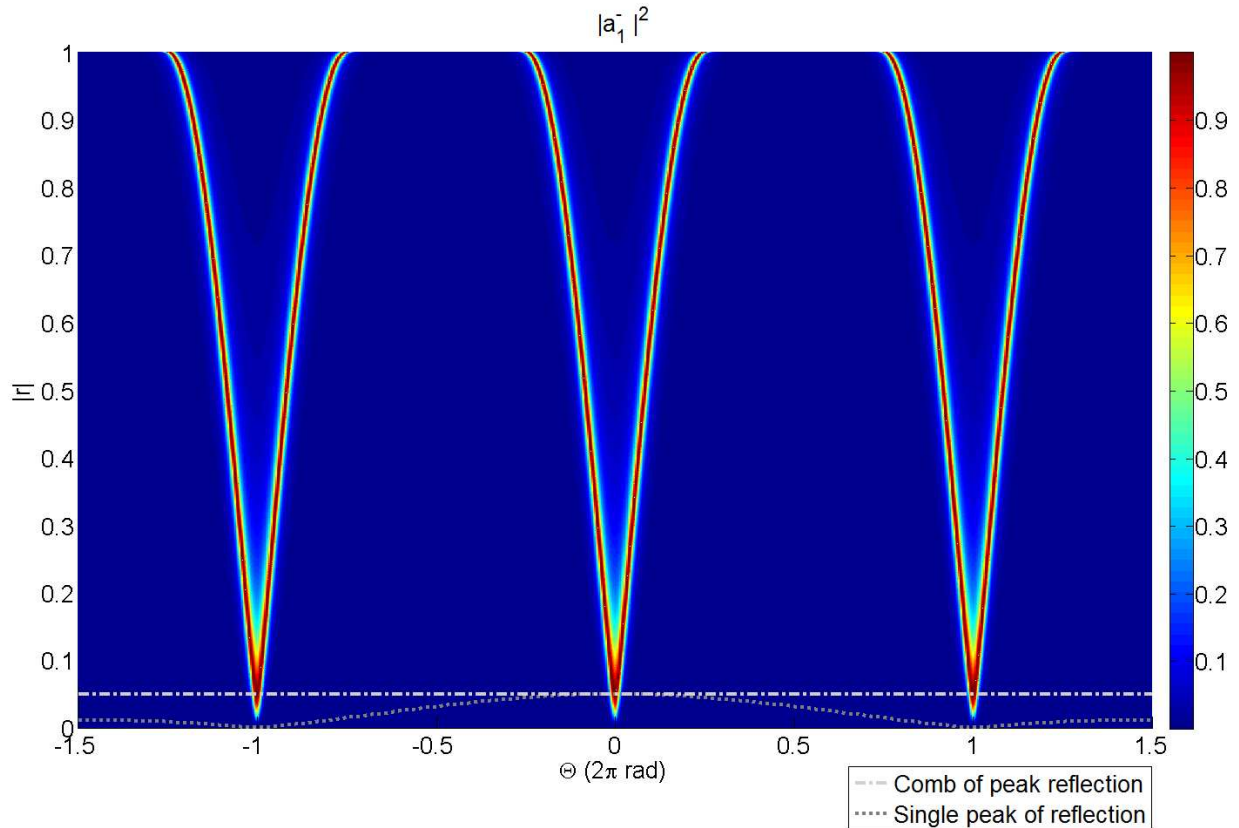
Figure 3.2: Spectral reflectivity of networks overlaid on the Θ - $|r|$ plane.

If we introduce a constant low reflectivity $|r| \approx 0.05$ for all β in the ring, we expect to see a comb of reflection peaks at every resonance condition $\Theta = 2m\pi$. Instead, if we want to realize an ultra-wide FSR mirror, we simply need to insert a network such that its reflectivity nulls line up at detuned resonance conditions, *i.e.*, $|r(\Theta = 2m\pi)| \approx 0.05\delta_{0,m}$, as depicted in gray lines in Fig. 3.2.

For higher values of κ^2, we observe an increase in the FWHM, as expected from Eq. (2.26). Similarly, the FWHM increases as the propagation loss in the ring increases, *i.e.*, α^2 decreases. In this case, the maximum reflection from the integrated microring one can obtain is no longer unity; more detailed analysis is presented in the next section. Figure 3.3 compares the plots for different values of κ^2 and α^2. Because the overall shapes of the response spectra are identical, I will mainly discuss the case where $\kappa^2 = 0.1$ and $\alpha^2 = 1$ for simplicity, but one can apply the analysis presented in this thesis to arbitrary values of the parameters as well.
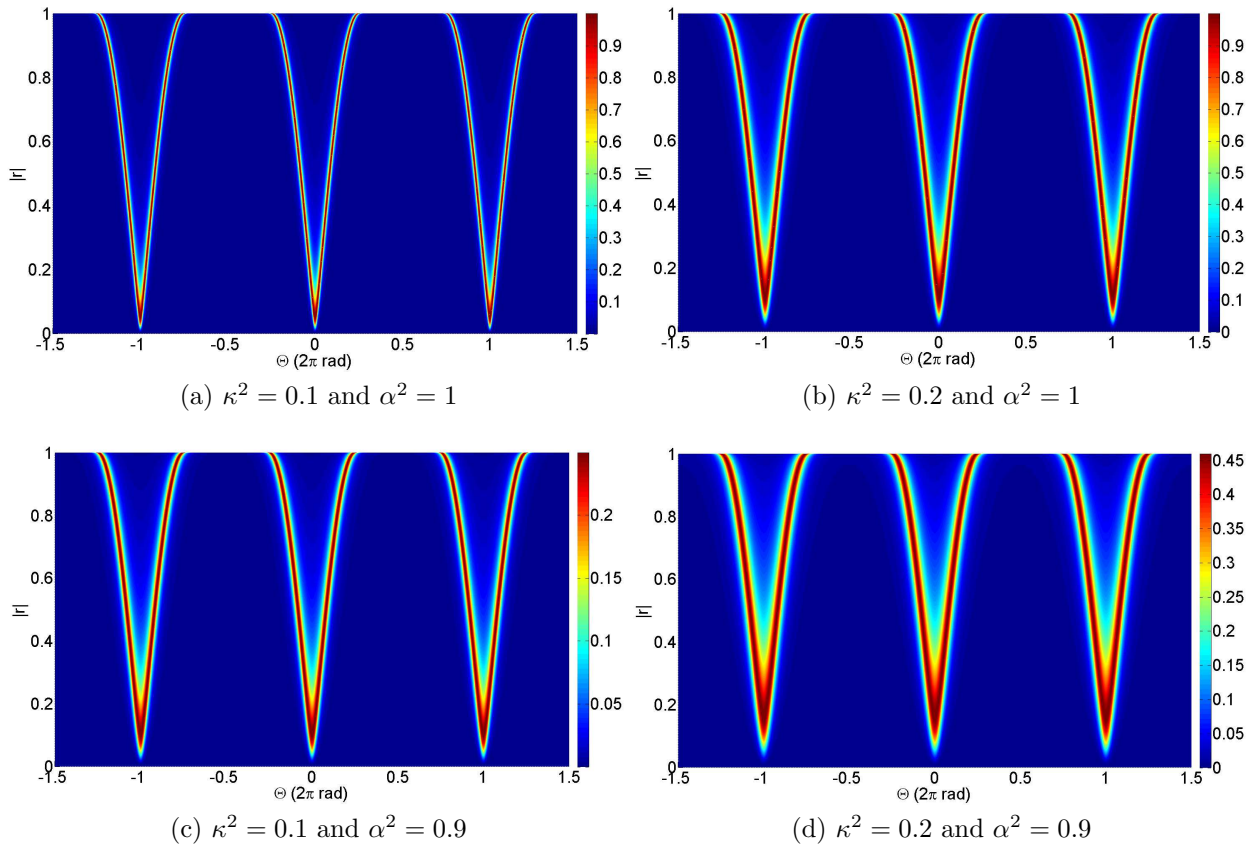
(a) $\kappa^2 = 0.1$ and $\alpha^2 = 1$

(b) $\kappa^2 = 0.2$ and $\alpha^2 = 1$

(c) $\kappa^2 = 0.1$ and $\alpha^2 = 0.9$

(d) $\kappa^2 = 0.2$ and $\alpha^2 = 0.9$

Figure 3.3: Comparison of the 3D reflection spectra of the integrated microring for different values of κ^2 and α^2. Note the changes in the color code scales for lossy cases.

3.3 Maximum Reflection Condition

In order to find the reflectivity of the network such that the reflection from the microring is maximum, we need to solve

$$\nabla_{\Theta,|r|}|a_1^-(\Theta,|r|)| = \mathbf{0}, \tag{3.8}$$

which yields the scattering element's critical reflectivity amplitude and the resultant microring reflection amplitude

$$|r_c(\Theta)| = \frac{\sqrt{(1+\alpha^2\tau^2)^2 - 4\alpha^2\tau^2\cos^2\Theta}}{1+\alpha^2\tau^2} \qquad \text{for} \quad -\frac{\pi}{2} \leq \Theta - 2m\pi \leq \frac{\pi}{2}, \tag{3.9}$$

$$|a_{1c}^-| = \frac{\alpha(1-\tau^2)}{1-\alpha^2\tau^2} \qquad \text{for} \quad -\frac{\pi}{2} \leq \Theta - 2m\pi \leq \frac{\pi}{2}, \tag{3.10}$$

respectively. Equation (3.9) corresponds to the maximum contour lines (dark red) of Fig. 3.3. At the resonance condition $\Theta = 2m\pi$, Eq. (3.9) reduces to

$$|r_c| = \frac{1-\alpha^2\tau^2}{1+\alpha^2\tau^2}. \tag{3.11}$$

Figure 3.4 graphs the critical reflection of the scattering element and the resultant microring reflection on the κ^2 - α^2 plane. For $\kappa^2 = 0.1$ and $\alpha^2 = 1$ as in the above example, we obtain $|r_c| = 0.0526$ and $|a_{1c}^-| = 1$, which agrees with what we observed in Fig. 3.2 and Fig. 3.3. Note that for $\alpha^2 = 1$ and $\kappa^2 << 1$, Eq. (3.9) reduces to $\kappa^2 = 2|r_c|$ as presented in [3].

For $|r| > |r_c|$, we observe the resonance phase condition starts to split as the scattering increases. This phenomenon can be best explained by considering the effective ring circumference. Due to reflection from the scattering element, the wave circulating in the ring can be resonant either by one complete round trip $(e^{j\Theta})$ in the low reflection limit $|r| \approx 0$, or two round trips $(e^{j2\Theta})$ in the high reflection limit $|r| \approx 1$, as depicted in Fig. 3.5. We hence observe that the FSR of the integrated microring reduces by half when a highly reflective scattering element is inserted.

In practice, it may be more difficult to control the coupling coefficient κ than the reflection $|r|$ because κ is exponentially dependent on the coupling gap between the ring and the bus waveguides, and a typical dimension of the gap is in the order of 50 to 100 nm. Figure 3.6
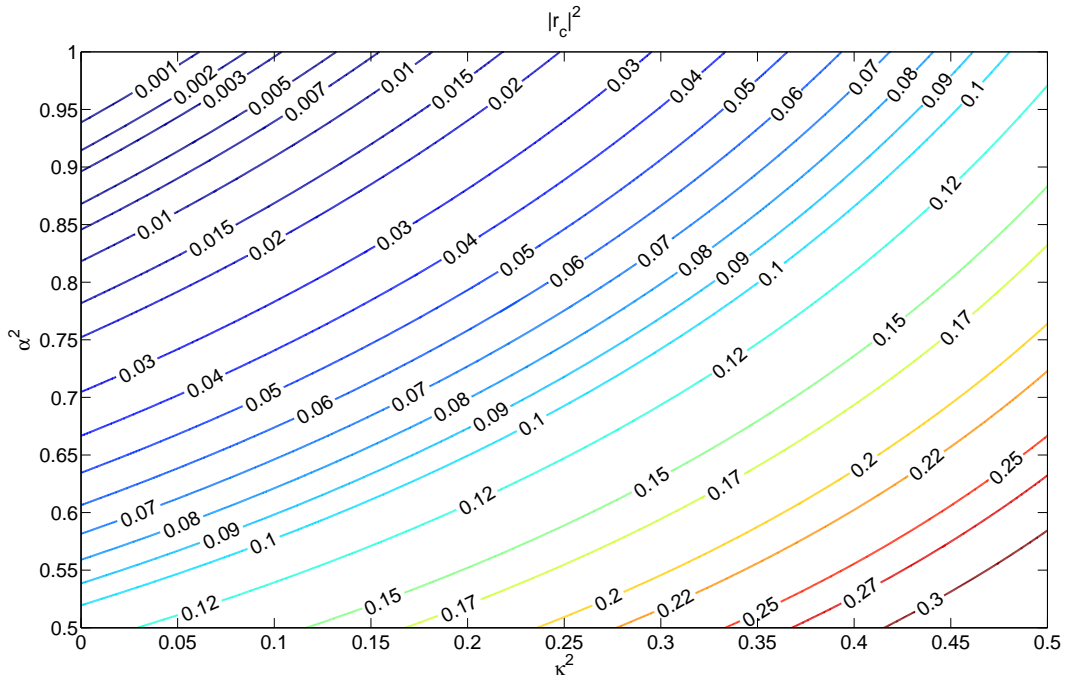
(a) Critical Reflection Condition
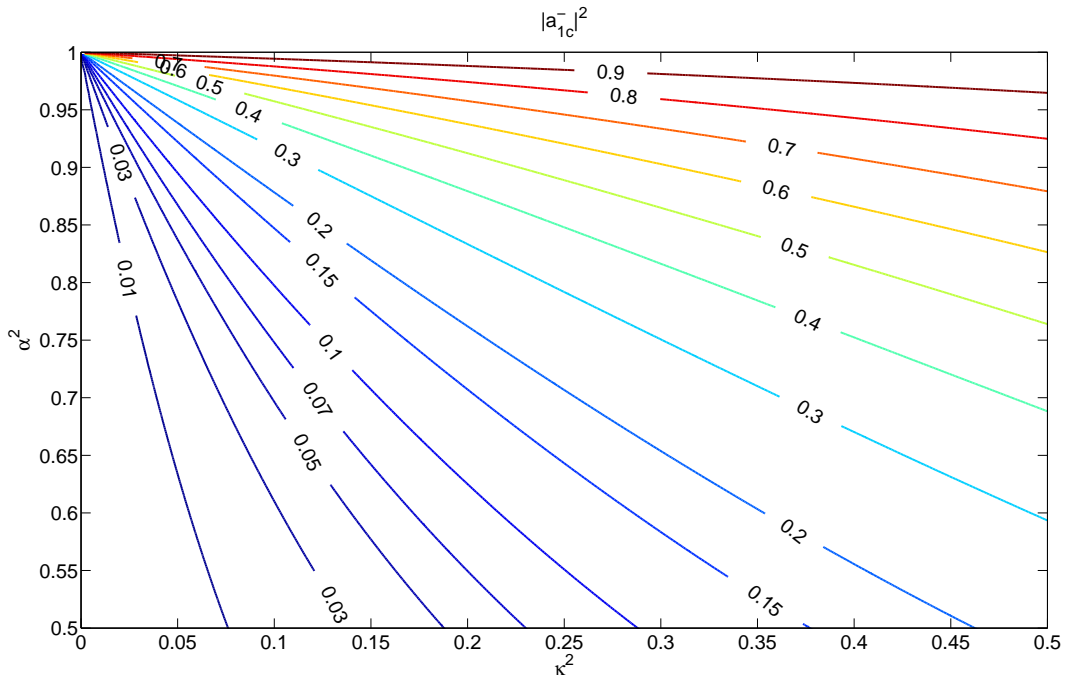
(b) Resultant reflection

Figure 3.4: Contour maps of critical reflection intensity and resultant microring reflection intensity in the κ^2 - α^2 plane.
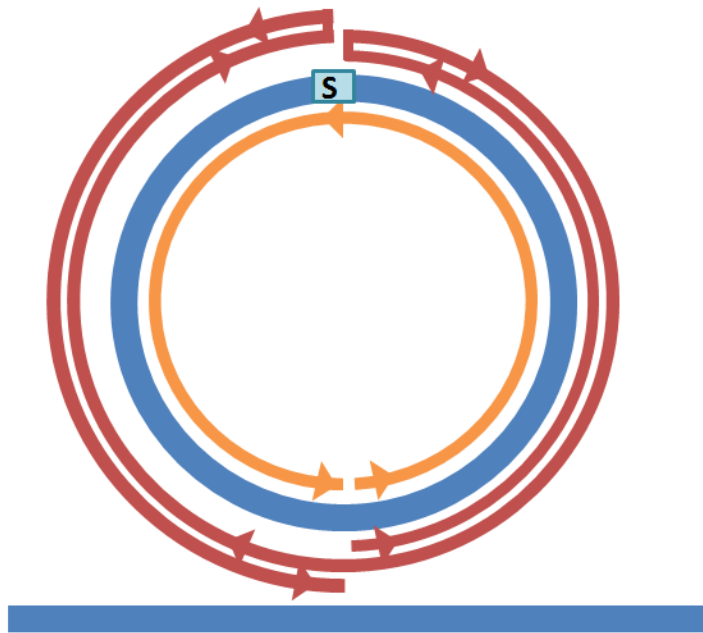
Figure 3.5: The wave in the ring can be resonant by making one round trip (orange, inner) or two round trips (red, outer). The effective resonant path is therefore a combination of the two.
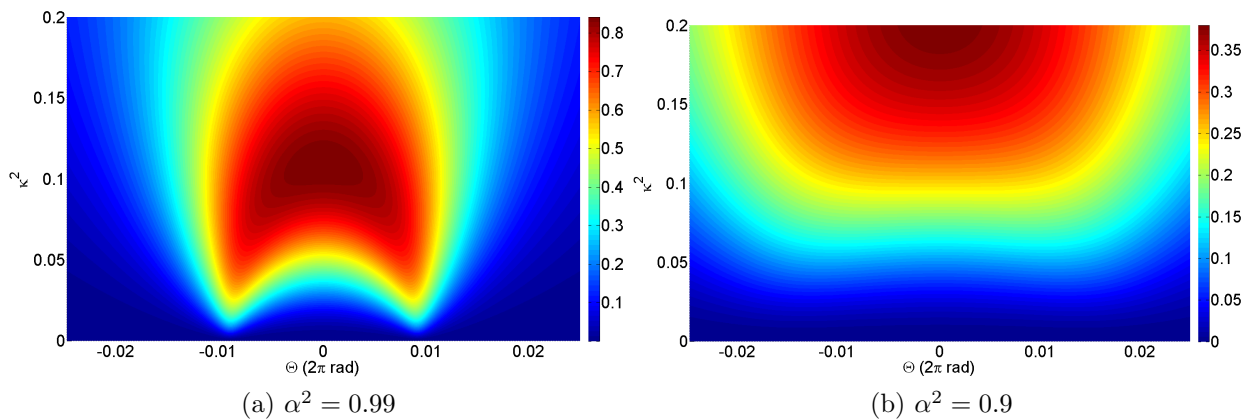

(a) $\alpha^2 = 0.99$

(b) $\alpha^2 = 0.9$

Figure 3.6: Sensitivity contour maps on the Θ - κ^2 plane. The graphs are plotting the reflection power of the microring for fixed $|r| = 0.0576$ or 0.105 for a range of κ^2 under two lossy conditions.

shows contour maps of the reflection power for fixed $|r|$ on the Θ - κ^2 plane. Here, κ_0 is the design coupling coefficient, and we assume that $|r| = r_c = 0.0576$ or 0.105 is a constant value optimized for $\kappa_0^2 = 0.1$, and $\alpha^2 = 0.99$ or 0.9, respectively. From the graphs, we see that a slightly larger coupling coefficient than the designed one is acceptable as expected from Fig. 3.4b, but a lower coupling coefficient may degrade the device performance. In the case of a low loss $\alpha^2 = 0.99$ as in Fig. 3.6a, we find that the range of $0.05 \leq \kappa^2 \leq 0.2$ will result in at least 50% of reflection power at resonance. Note that the maximum value of reflection is obtained for κ^2 larger than $\kappa_0^2 = 0.1$ in the figure. This is because for a lossy structure, an increase in the coupling coefficient κ and corresponding increase in $|r| = r_c$ will monotonically increase the maximum reflection $|a_{1c}^-|^2$. However, an increase in the value of κ will widen the FWHM of the microring resonator given in Eq. (2.27).

3.4   Null Transmission Condition

When the entire structure is lossless, the energy conservation law requires that the sum of reflected and transmitted power equal to the input power, $i.e.$, $|a_1^-|^2 + |b_1^+|^2 = |a_1^+|^2 = 1$. Therefore, the maximum reflection condition given in Eq. (3.9) coincides the null transmission condition for $\alpha^2 = 1$. For lossy case, we solve

$$|b_1^+(\Theta, r_{nt})| = 0, \tag{3.12}$$

which yields the solution of the inserted network's reflection coefficient

$$r_{nt} = \frac{\sqrt{(\alpha^2 - \tau^2)(1 - \alpha^2\tau^2)}}{\alpha(1 + \tau^2)} \qquad \text{for } \tau^2 \leq \alpha^2 < 1, \ \Theta = 2m\pi. \tag{3.13}$$

Unlike the maximum reflection condition where the solution $|r_c(\Theta)|$ exists for a wide range of Θ, the null transmission can be achieved only at the resonance conditions $\Theta = 2m\pi$ when $\alpha^2 < 1$. In addition, the null transmission condition also requires that the loss of the structure satisfy $\tau^2 \leq \alpha^2 \leq 1$. Note that Eq. (3.13) reduces to the critical coupling condition $\alpha = \tau$ [19] in the case where no reflective element is introduced, $i.e.$, $r_{nt} = 0$.

3.5 Comb of Peak Reflector Configuration

From Fig. 3.2, we saw that in order to realize periodic reflection peaks we can introduce a flat band reflective element in the microring. In practice, we can insert a quarter-wavelength FP network to a microring (FP-MRR). In Section 2.4, we found that the transmission of a given FP network is given by

$$t_{FP} = \frac{t_{int}^2 e^{j\theta_d}}{1 - r_{int}^2 e^{j2\theta_d}} = |t_{FP}|e^{j\theta_{FP}}, \qquad (3.14)$$

and the reflection is given by

$$r_{FP} = \frac{-r_{int}(1 - e^{j2\theta_d})}{1 - r_{int}^2 e^{j2\theta_d}} \qquad (3.15)$$

where r_{int} and t_{int} are reflection and transmission coefficients at the FP-ring interface, respectively.

In typical low-contrast resonators, $|r_{int}|^2 << 1$, so Eq. (3.14) reduces to

$$t_{FP} \approx t_{int}^2 e^{j\theta_d}. \qquad (3.16)$$

Equation (3.16) and Eq. (2.34) indicate that the transmission phase shift of a low reflection FP network is roughly a linear function of β with the slope equal to its length d. We thus obtain the transmission phase shift in the network $\theta_{FP} \approx \theta_d$, and therefore the total round trip detuned phase in the integrated ring is $\Theta = \theta + \theta_{FP} - \beta_0 L_t \approx (\beta - \beta_0)L_t$.

For $d = \frac{1}{4}\lambda_{0,e}$, where $\lambda_{0,e}$ is the effective wavelength at the design frequency, we obtain $\theta_d = \frac{\pi}{2}$, and Eq. (3.15) reduces to

$$r_{FP} = \frac{-2r_{int}}{1 + r_{int}^2}, \qquad (3.17)$$

and therefore we design r_{int} such that $|r_{FP}| = r_c$ in order to obtain the maximum reflection from the microring. Because $\frac{\partial\theta}{\partial\beta} >> \frac{\partial\theta_d}{\partial\beta}$ for a microring with its circumference $L >> d$, we can effectively model the reflection from the FP network as a constant value:

$$|r(\Theta)| \approx r_c \qquad (3.18)$$

near the design wavelength.

Figure 3.7a shows plots of the reflection intensity for different values of α^2 and fixed value of $\kappa^2 = 0.9$. We observe periodic peak reflectance at each resonance condition $\Theta = 2m\pi$ as expected. Note that the spectral response resembles that of a sampled grating distributed Bragg reflector (SGDBR) plotted in Fig. 3.7b, which is widely used for mirrors in quasi-continuous tunable lasers. In a SGDBR, many quarter-wavelength FP networks are cascaded in order to realize high reflectance. In the case of FP-MRR, we make use of field build-up in the ring resonator to amplify the small reflection introduced from a single or a few FP elements, which effectively reduces the size and fabrication effort of the periodic-peak mirror. In addition, for the FP-MRR we do not observe any side mode peaks that are present in the SGDBR [24], which degrades single mode operation of semiconductor lasers.

3.6   Single Peak Reflector Configuration

In order to realize a single peak reflection only at the design resonance condition $\Theta = 0$, we must insert a network such that it introduces no reflection at detuned resonance conditions, i.e.,

$$r(\Theta) = 0 \qquad \text{for all } \Theta = 2m\pi, \; m \text{ is nonzero integer.} \tag{3.19}$$

One element that realizes such condition is a Bragg grating or DBR, which consists of a large number, say $2N$, of quarter-wavelength FP elements cascaded together. The total length of such grating is $L_g = \frac{N}{2}\lambda_{0,e}$. In the low reflectivity limit, we may neglect multiple reflection in the grating and obtain transmissivity and reflectivity [20, Ch. 3],
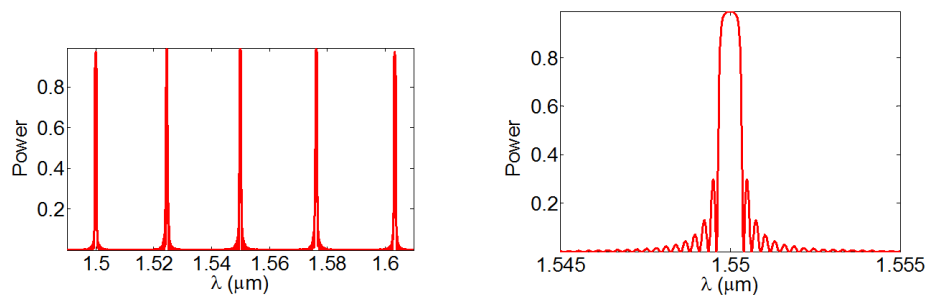
$$t_g \;=\; t_{int}^{2N} e^{j\theta_g} \tag{3.20}$$

$$|r_g| \;=\; 2N|r_{int}\frac{\sin\theta_g}{\theta_g}|, \qquad N|r_{int}| < 0.2 \tag{3.21}$$

$$\theta_g \;=\; (\beta - \beta_0)L_g \tag{3.22}$$

where r_{int} is again the reflection coefficient at each interface in the grating, and θ_g is the detuned phase change in the grating. Intuitively, the magnitude of the reflectivity peak
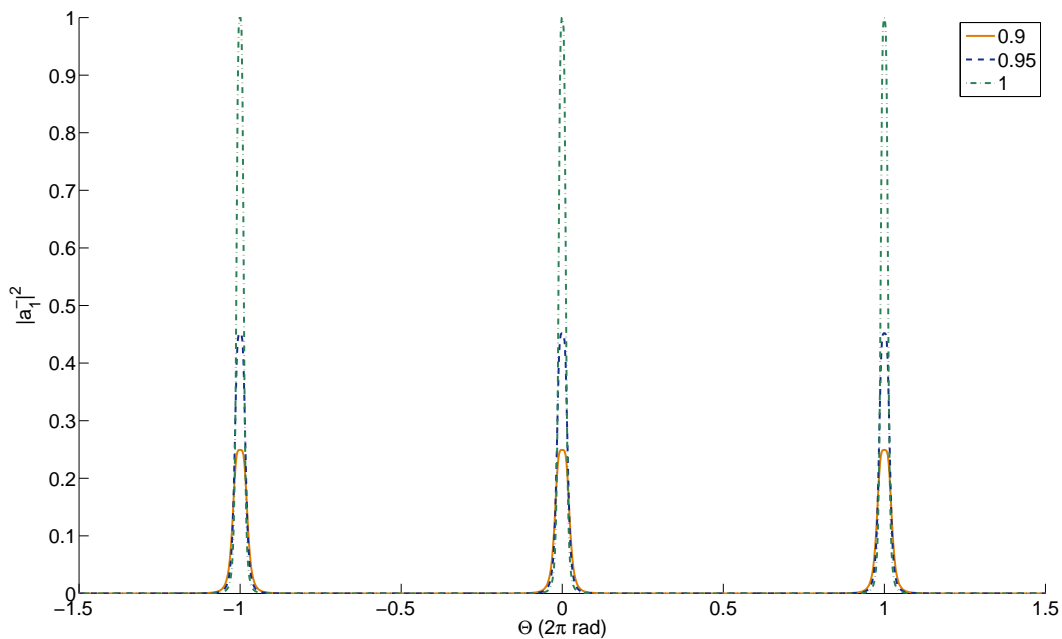
(a) Reflectance spectra of FP-MRR for various values of α^2 at fixed $\kappa^2 = 0.9$.

(b) Reflectance spectra of a SGDBR consisting of 90 bursts of 10-pair Bragg grating with material index contrast $(n_1, n_2) = (3, 2.99)$. The burst period is $30\lambda_{0,e}$ where the $\lambda_0 = 1550$ nm. The zoomed in graph (right) shows side peaks near its main peak.

Figure 3.7: Comparison of reflectance spectra of FP-MRR and SGDBR. Note the absence of side mode reflection peaks near the main peaks for the FP-MRR.

should approach $2N|r_{int}|$ at the design frequency because each pair of FP elements has two reflection interfaces.

To achieve maximum reflection condition, we first choose the combination of r_{int} and N such that

$$2N|r_{int}| = r_c. \tag{3.23}$$

Next, we observe that

$$\Theta = (\beta - \beta_0)L_t = (\beta - \beta_0)(L + L_g) \tag{3.24}$$

where $L_t = L + L_g$ is the circumference of the grating and the ring. We define the ratio of the detuned phases as $p = \frac{\theta_g}{\Theta}$, and from Eqs. (3.22) and (3.24), we obtain

$$0 \; < \; p = \frac{L_g}{L + L_g} \; \leq \; 1. \tag{3.25}$$

Note that p is fixed for a given geometry of the structure. Substituting Eq. (3.25) into Eq. (3.21) yields

$$|r_g(\Theta)| = 2N|r_{int}\frac{\sin{(p\Theta)}}{p\Theta}|. \tag{3.26}$$

Imposing Eq. (3.19) on Eq. (3.26) results in

$$\sin{(p\Theta)} \; = \; 0 \qquad \text{for all } \Theta = 2m\pi, \; m \text{ is nonzero integer,} \tag{3.27}$$

$$2mp\pi \; = \; n\pi \qquad \text{for some integer } n, \tag{3.28}$$

$$p \; = \; \frac{n}{2m} \qquad \text{is fixed for any } m. \tag{3.29}$$

The possible choices of n satisfying Eqs. (3.25) and (3.29) are $n = m$ or $n = 2m$, and therefore we obtain $p = \frac{1}{2}$ or $p = 1$, respectively. The corresponding grating lengths are

$$L_g = L = \frac{1}{2}L_t \qquad \text{or} \qquad L_g = L_t, \; L = 0. \tag{3.30}$$

Physically, the first case is where exactly half of the ring consists of grating (Fig. 3.8a), and the second case is where the entire ring consists of grating (Fig. 3.8b). These two cases are the only configurations that will suppress reflection peaks at detuned resonances, *i.e.*,
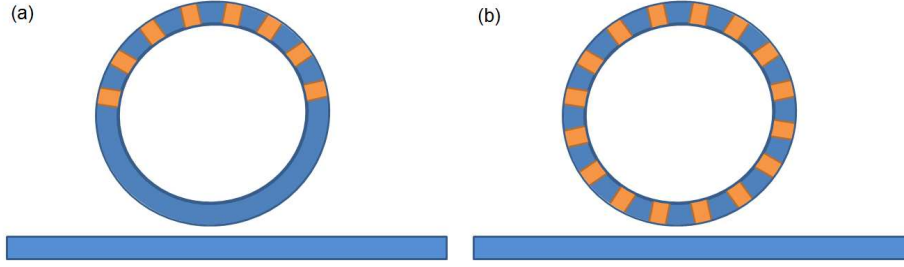
Figure 3.8: Schematic diagrams of single-peak reflector configurations using DBR grating in the microring. (a) Half DBR-MRR. (b) Full DBR-MRR.
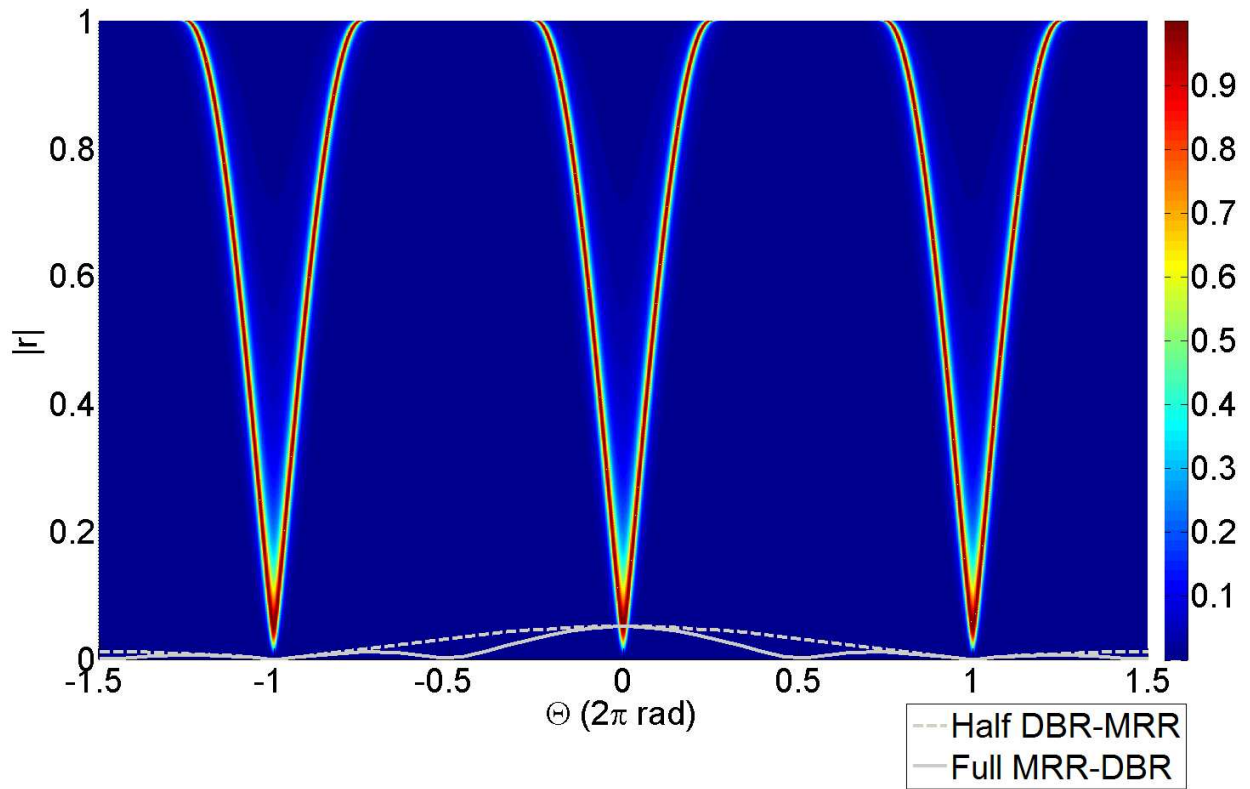
$\Theta = 2m\pi$ where m is nonzero integer.

Figure 3.9: Two DBR-MRR configurations reflectivity spectra and reflection spectra overlaid on the Θ - $|r|$ plane.

Figure 3.9 depicts the two DBR-MRR configurations' reflectivity spectra and the microring's reflection spectra overlaid on the Θ - $|r|$ plane. Figure 3.10 plots the resultant reflection spectra of the DBR-MRRs. We observe only a single peak at the design frequency as desired. Note that the full DBR-MRR's $|r_{int}|$ should be approximately one half the corresponding
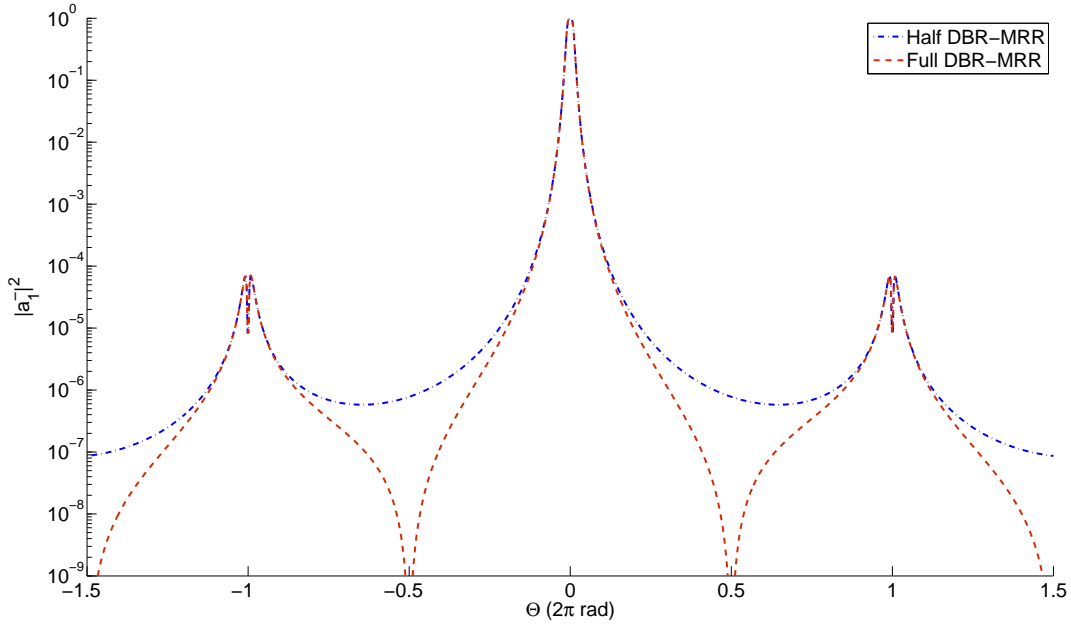
Figure 3.10: Reflection spectra of the two single-peak DBR-MRR configurations.

value in the half DBR-MRR in order to satisfy Eq. (3.23); there are twice more reflection interfaces for the full DBR-MRR than for the half DBR-MRR.

3.7   Ultra-Narrow Transmission Filter

In this section, I will discuss the case of a FP element inserted microring where the mirror reflectivity of the FP element is significant. Such element can be effectively realized by employing a DBR etalon structure, which consists of a DBR grating as the end mirrors. This DBR etalon integrated microring structure will be referred to as DBR-E-MRR, and its schematic diagram is drawn in Fig. 3.11.
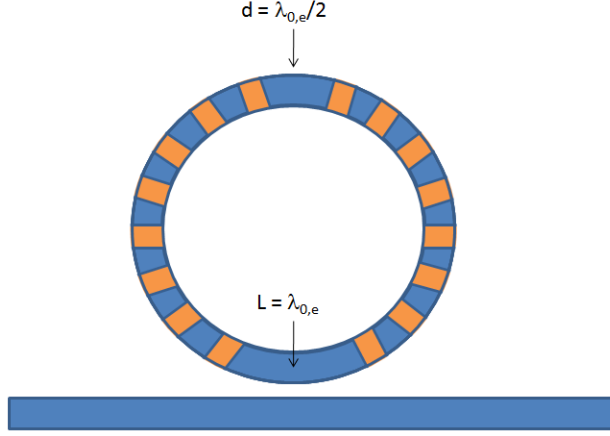
Figure 3.11: Schematic diagram of a DBR-E-MRR. d is the length of the DBR etalon, and L is the length of the microring excluding the scattering element.

For analysis, we start by re-writing Eq. (3.14) and Eq. (3.15) as

$$t_{FP} = \frac{t_g^2 e^{j\theta_d}}{1 - r_g^2 e^{j2\theta_d}} = \frac{t_g^2 (e^{j\theta_d} - r_g^2 e^{-j\theta_d})}{1 - 2r_g^2 \cos 2\theta_d + r_g^4} = |t_{FP}| e^{j\theta_{FP}} \quad (3.31)$$

$$r_{FP} = \frac{-r_g(1 - e^{j\theta_d})}{1 - r_g^2 e^{j2\theta_d}} \quad (3.32)$$

$$|r_{FP}|^2 = \frac{r_g^2(2 - 2\cos 2\theta_d)}{1 - 2r_g^2 \cos 2\theta_d + r_g^4} = \frac{4r_g^2(1 - \cos^2 \theta_d)}{(1 + r_g^2)^2 - 4r_g^2 \cos^2 \theta_d} \quad (3.33)$$

where r_g and t_g are the effective mirror reflectivity from the grating. At the design wavelength, we have [20, Ch. 3]

$$r_g = \tanh\left(N \ln\left(\frac{1 + r_{int}}{1 - r_{int}}\right)\right), \quad (3.34)$$

and $t_g = \sqrt{1 - r_g^2}$ for the lossless case. The phase of the transmission coefficient of the etalon t_{FP} and its derivative can be solved from Eq. (3.31):

$$\theta_{FP} = \arctan\left(\Gamma \tan \theta_d\right) \quad (3.35)$$

$$\frac{\partial \theta_{FP}}{\partial \theta_d} = \frac{\Gamma \sec^2 \theta_d}{1 + \Gamma^2 \tan^2 \theta_d}, \quad (3.36)$$

where $\Gamma = \frac{1 + r_g^2}{1 - r_g^2}$. We re-write Eq. (3.35) as $\theta_d = \arctan\left(\frac{1}{\Gamma} \tan \theta_{FP}\right)$, and plugging it into

Eq. (3.33) yields

$$|r_{FP}| = \frac{2r_g \tan\theta_{FP}}{\sqrt{(1 + r_g^2)^2(\tan^2\theta_{FP} + \Gamma^2) - 4\Gamma^2 r_g^2}}, \tag{3.37}$$

where the trig identity $\cos(\arctan x) = \frac{1}{\sqrt{1+x^2}}$ has been used.

For $r_g \approx 1$ and $d = \frac{\lambda_{0,e}}{2}$, we obtain $\frac{\partial\theta_{FP}}{\partial\beta} = \Gamma d >> \frac{\partial\theta}{\partial\beta} = L$ near the design wavelength. This condition implies that θ is a slowly varying function compared to θ_{FP}, and therefore we can approximate $\Theta(\beta) = \theta(\beta) + \theta_{FP}(\beta) - \beta_0 L_t \approx \theta_{FP}(\beta) + 2\pi - \beta_0 L_t$ near the design wavelength because $\theta(\beta_0) = \beta_0 L = \beta_0 \lambda_{0,e} = 2\pi$ is the phase shift from the ring portion of length $L = \lambda_{0,e}$. Note that $\beta_0 L_t = 2m\pi$ for some integer m by designing the total circumference $L_t = m\lambda_{0,e}$. By plotting Eq. (3.37) on the Θ - $|r|$ plane, we can anticipate the spectral response of the DBR-E-MRR structure. Note that in the analysis, we are assuming that r_g is a constant value near the design wavelength given by Eq. (3.34); in reality, the value of r_g will change, and one can employ the transfer matrix method discussed in Section 2.5 to more accurately evaluate the spectral reflection of the DBR etalon structure.

Figure 3.12a plots Eq. (3.37) on top of the colored contour graph near the design wavelength for $r_g = 0.99$. Because $|r| = 0$ at the design wavelength, we expect to see a very narrow linewidth transmission at the design wavelength until it intersects with the critical reflection condition r_c (red color). Because r_c is typically very small, we expect to observe that the FWHM of the DBR-E-MRR is much smaller than that of the etalon. Figure 3.12b compares the transmission spectra of the two structures. Note that $2\delta\Theta_{DBR-E-MRR} \approx 0.02 << 2\delta\Theta_{Etalon} \approx 0.25$.

3.8 Sharp Cut-Off Mirror

If we slightly detune the etalon length $d' = d + \delta$ and the ring-only length $L' = L - \delta$, then we expect to see the spectral reflection of $|r(\Theta)|$ shift horizontally on the Θ - $|r|$ plane, as seen in Fig. 3.13a. From the graph, we expect to see a sharp transition between 100% reflection to 100% transmission near the design wavelength for the lossless case. Figure 3.13b shows the reflection and transmission power of the detuned DBR-E-MRR structure. As anticipated, we realize a sharp cut-off mirror near the design wavelength. This could have applications
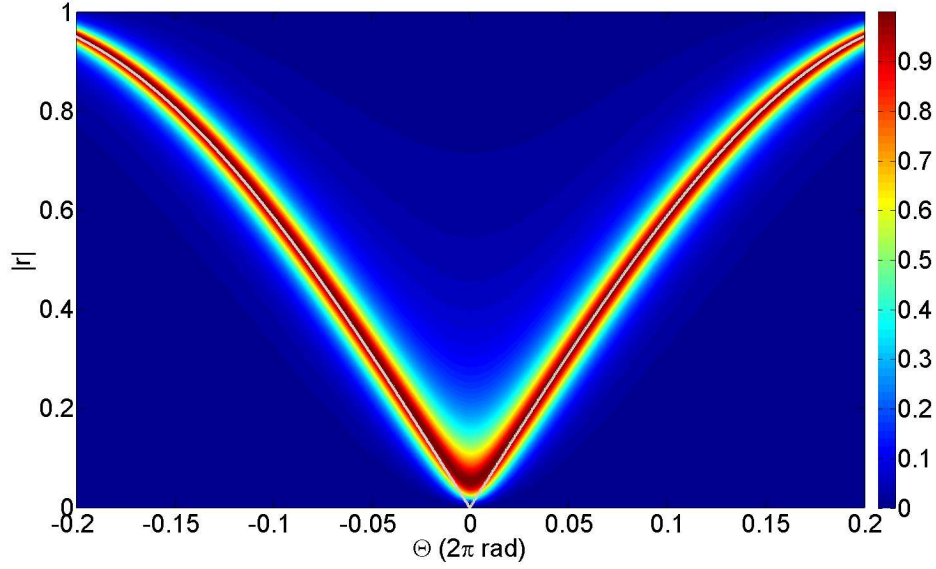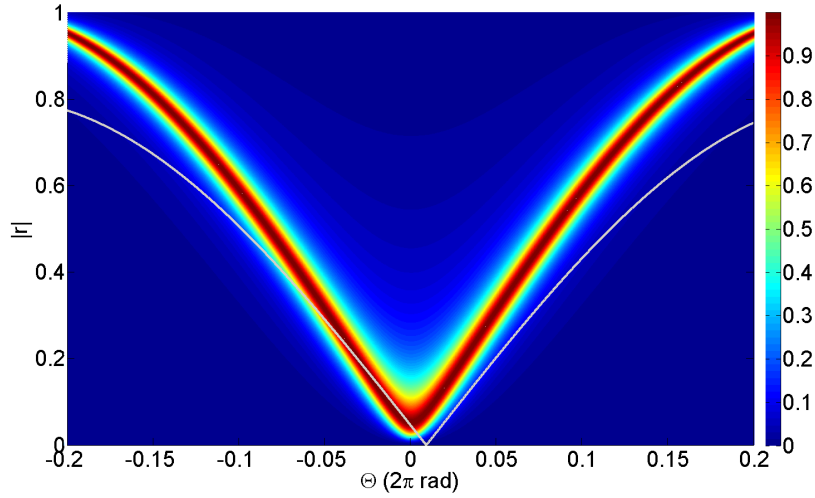
(a) Reflection spectrum of DBR etalon on the Θ - $|r|$ plane for $r_g = 0.99$ under lossless condition.
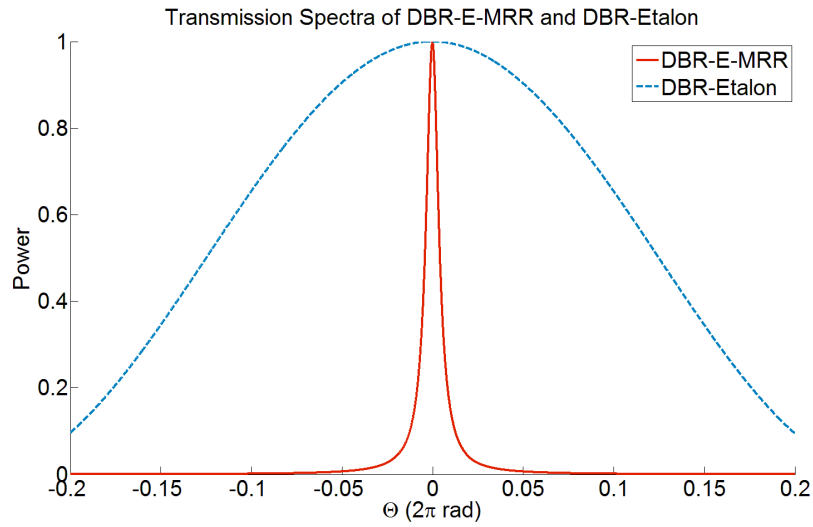
(b) Transmission spectra of the DBR-E-MRR and its etalon structure under lossless condition.

Figure 3.12: Ultra-narrow transmission filter employing DBR etalon in the microring. Notice the significant narrowing of the linewidth for the DBR-E-MRR.

(a) Reflection spectrum of detuned DBR etalon on the Θ - $|r|$ plane for $r_g = 0.5$ under lossless condition.
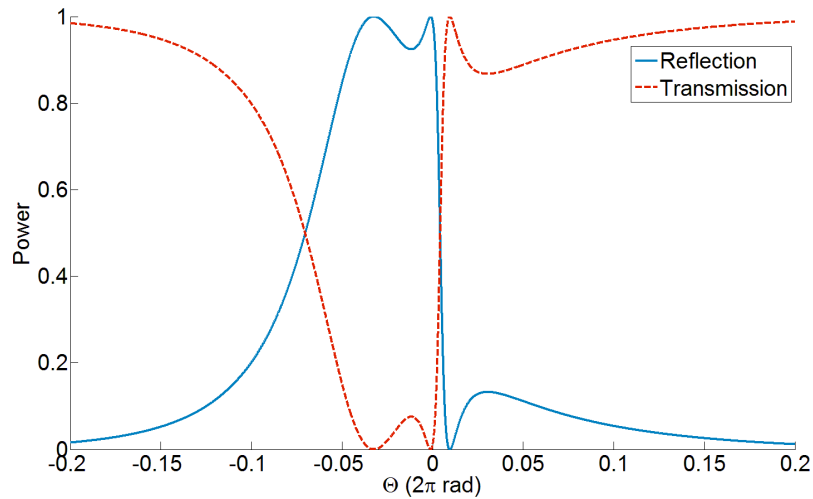
(b) Reflection and transmission spectra of the detuned DBR-E-MRR under lossless condition.

Figure 3.13: Sharp cut-off mirror configuration of the DBR-E-MRR by slightly detuning the etalon length d.

in optical switching. In practice, it will be a technical challenge to accurately resolve a very small detuning length δ.

CHAPTER 4

CONCLUSION

4.1 Achievements

In this thesis, I presented a semi-analytic model of the microring resonators with integrated scattering elements. When a scattering element is introduced in the ring resonator, two modes of waves propagating in the opposite directions in the ring are coupled. By engineering the reflectivity spectrum of the inserted element, one can obtain a mirror with series of peak reflection or a single-peak reflections. Its compact structure and flexible design make it a good candidate for in-plane mirrors, filters, and switches for photonic integrated circuits.

4.2 Future Directions

The modeling presented in the thesis assumes that numerical values of structure parameters, such as the coupling coefficient κ, propagation loss in the ring α, modal index n_e, and reflection spectrum of the inserted network r, are precisely known. In practice, these parameter values cannot be determined, simulated, or fabricated with exact precision. It is therefore desired to study the sensitivity analysis of the structure's reflection spectrum for a given deviation in the parameter values. In addition, developing recipes to fabricate the devices that fall within operational range of target physical dimensions and material properties needs to be done. Lastly, measurement, testing, and analysis of the devices is also very important for realization of the microring structures presented in the thesis.

APPENDIX A

SCATTERING MATRIX PROPERTIES

A.1 General Case

For a four-port network of normalized fields, inputs x_1, x_2 and outputs y_1, y_2 can be related by a general scattering matrix $\mathbf{S}$,

$$\begin{bmatrix} y_1 \\ y_2 \end{bmatrix} = \mathbf{S} \begin{bmatrix} x_1 \\ x_2 \end{bmatrix} = \begin{bmatrix} S_{11} & S_{12} \\ S_{21} & S_{22} \end{bmatrix} \begin{bmatrix} x_1 \\ x_2 \end{bmatrix} \tag{A.1}$$

where $S_{kl} = |S_{kl}|e^{j\phi_{kl}}$ and $0 \leq \phi_{kl} < 2\pi$ is the phase of the corresponding element S_{kl}. To accurately characterize a given network, we need to define eight nonnegative real variables, four magnitude terns $|S_{kl}|$ and four phase terms ϕ_{kl}.

A.2 Reciprocal Case

Reciprocity of a network imposes a condition on a scattering matrix

$$\mathbf{S}^T = \mathbf{S}, \tag{A.2}$$

which simply yields,

$$S_{12} = S_{21}. \tag{A.3}$$

Thus, a scattering matrix of a reciprocal network has the general form

$$\mathbf{S} = \begin{bmatrix} S_{11} & S_{12} \\ S_{12} & S_{22} \end{bmatrix}. \tag{A.4}$$

A.3 Lossless Case

The sum of input power is given by

$$|x_1|^2 + |x_2|^2 = \begin{bmatrix} x_1 \\ x_2 \end{bmatrix}^\dagger \begin{bmatrix} x_1 \\ x_2 \end{bmatrix}, \tag{A.5}$$

and similarly the sum of output power is given by

$$|y_1|^2 + |y_2|^2 = \begin{bmatrix} y_1 \\ y_2 \end{bmatrix}^\dagger \begin{bmatrix} y_1 \\ y_2 \end{bmatrix} = \left(\mathbf{S} \begin{bmatrix} x_1 \\ x_2 \end{bmatrix} \right)^\dagger \left(\mathbf{S} \begin{bmatrix} x_1 \\ x_2 \end{bmatrix} \right) = \begin{bmatrix} x_1 \\ x_2 \end{bmatrix}^\dagger \mathbf{S}^\dagger \mathbf{S} \begin{bmatrix} x_1 \\ x_2 \end{bmatrix}. \tag{A.6}$$

If a network is lossless, the sum of input power must equal to the sum of output power. Equating Eq. (A.5) and Eq. (A.6), we obtain a constraint on the scattering matrix,

$$\mathbf{S}^\dagger \mathbf{S} = \mathbf{I}, \tag{A.7}$$

which then yields the following three conditions:

$$|S_{11}|^2 + |S_{21}|^2 = 1 \tag{A.8}$$

$$|S_{12}|^2 + |S_{22}|^2 = 1 \tag{A.9}$$

$$S_{11}^* S_{12} + S_{21}^* S_{22} = 0. \tag{A.10}$$

Equations (A.8), (A.9), and (A.10) each give a constraint to a magnitude term, and Eq. (A.10) gives an additional constraint to a phase term. Simplifying the constraints results in

$$|S_{12}| = \sqrt{1 - |S_{11}|^2} \tag{A.11}$$

$$|S_{21}| = \sqrt{1 - |S_{11}|^2} \tag{A.12}$$

$$|S_{22}| = |S_{11}| \tag{A.13}$$

$$\phi_{11} + \phi_{22} = \phi_{12} + \phi_{21} + m\pi, \tag{A.14}$$

where $m = \pm 1$ or ± 3. Applying these conditions to the scattering matrix $\mathbf{S}$, we obtain

$$\mathbf{S} = \begin{bmatrix} |r|e^{j\phi_{11}} & |t|e^{j\phi_{12}} \\ |t|e^{j\phi_{21}} & |r|e^{j\phi_{22}} \end{bmatrix} \tag{A.15}$$

$$= \begin{bmatrix} |r|e^{j\frac{\phi_{11}-\phi_{22}}{2}} & |t|e^{j(\phi_{12}-\psi)} \\ |t|e^{j(\phi_{21}-\psi)} & |r|e^{-j\frac{\phi_{11}-\phi_{22}}{2}} \end{bmatrix} e^{j\psi} \tag{A.16}$$

$$= \begin{bmatrix} |r|e^{j\phi_r} & |t|e^{j\frac{\phi_{12}-\phi_{21}-m\pi}{2}} \\ |t|e^{-j\frac{\phi_{12}-\phi_{21}-m\pi}{2}}e^{-jm\pi} & |r|e^{-j\phi_r} \end{bmatrix} e^{j\psi} \tag{A.17}$$

$$= \begin{bmatrix} |r|e^{j\phi_r} & |t|e^{j\phi_t} \\ -|t|e^{-j\phi_t} & |r|e^{-j\phi_r} \end{bmatrix} e^{j\psi} \tag{A.18}$$

$$= \begin{bmatrix} r & t \\ -t^* & r^* \end{bmatrix} e^{j\psi}, \tag{A.19}$$

where $|r| = |S_{11}|$, $|t| = \sqrt{1-|S_{11}|^2}$, and $\psi = \frac{\phi_{11}+\phi_{22}}{2}$. Thus, a lossless condition on the network reduces the number of free variables of the scattering matrix to one magnitude variable $|r|$ and three phase variables ϕ_r, ϕ_t, and ψ.

A.4   Lossless Reciprocal Case

If a lossless network is also reciprocal, we impose an additional condition on Eq. (A.19) as follows:

$$t = -t^*. \tag{A.20}$$

From Eq. (A.20) we obtain $t = \pm j|t|$. The sign can be lumped into ϕ_r and ψ by adding π to each term. Therefore, a scattering matrix of a lossless reciprocal network is described by a general form

$$\mathbf{S} = \begin{bmatrix} r & j|t| \\ j|t| & r^* \end{bmatrix} e^{j\psi} = \begin{bmatrix} -j|r|e^{j\phi_r} & |t| \\ |t| & -j|r|e^{-j\phi_r} \end{bmatrix} e^{j(\psi+\frac{\pi}{2})}, \tag{A.21}$$

41

which is characterized by one magnitude term $|r|$ and two phase terms ϕ_r, ψ. Note that the transmission phase shift of the network is given by $\phi_{12} = \psi + \frac{\pi}{2}$.

REFERENCES

[1] V. Van, Philippe P. Absil, J. V. Hryniewicz, and P.-T. Ho, "Propagation loss in single-mode GaAs-AlGaAs microring resonators–measurement and model," *J. Lightwave Tech.*, **19**, pp. 1734 (2001).

[2] D.-X. Xu, A. Densmore, A. Delge, P. Waldron, R. McKinnon, S. Janz, J. Lapointe, G. Lopinski, T. Mischki, E. Post, P. Cheben, and J. H. Schmid, "Folded cavity SOI microring sensors for high sensitivity and real time measurement of biomolecular binding," *Opt. Exp.*, **16**, pp. 15137 (2008).

[3] B. E. Little, S. T. Chu, and H. A. Haus, "Second-order filtering and sensing with partially coupled traveling waves in a single resonator," *Opt. Lett.*, **23**, pp. 1570 (1998).

[4] J. E. Heebner, R. W. Boyd, and Q-H. Park, "SCISSOR solitons and other novel propagation effects in microresonator-modified waveguides," *J. Opt. Soc. Am. B*, **19**, pp. 722 (2002).

[5] A. M. Prabhu, H. L. Liew, and V. Van, "Generalized parallel-cascaded microring networks for spectral engineering applications," *J. Opt. Soc. Am. B*, **25**, pp. 1505 (2008).

[6] J. K. S. Poon, J. Scheuer, and A. Yariv, "Wavelength-selective reflector based on a circular array of coupled microring resonators," *IEEE Phot. Tech. Lett.*, **16**, pp. 1331 (2004).

[7] Y. M. Ladobasa, S. Darmawan, and M.-K. Chin, "Matrix analysis of 2-D microresonator lattice optical fields," *IEEE J. Quantum Electron.*, **41**, pp. 1410 (2005).

[8] L. Zhang, M. Song, T. Wu, L. Zou, R. G. Beausoleil, and A. E. Willner, "Embedded ring resonators for microphotonic applications," *Opt. Lett.*, **33**, pp. 1978 (2008).

[9] I. Chremmos and N. Uzunoglu, "Reflective properties of double-ring resonator system coupled to a waveguide," *IEEE Phot. Tech. Lett.*, **17**, pp. 2110 (2005).

[10] V. Van, "Dual-mode microring reflection filters," *J. Lightwave Tech.*, **25**, pp. 3142 (2007).

[11] O. Schwelb, "Band-limited optical mirrors based on ring resonators: analysis and design," *J. Lightwave Tech.*, **23**, pp. 3931 (2005).

[12] G. T. Paloczi, J. Scheuer, and A. Yariv, "Compact microring-based wavelength-selective inline optical reflector," *IEEE Phot. Tech. Lett.*, **17**, pp. 390 (2005).

[13] J. Scheuer, G. T. Paloczi, and A. Yariv, "All optically tunable wavelength-selective reflector consisting of coupled polymeric microring resonators," *Appl. Phys. Lett.*, **87**, 251102 (2005).

[14] Y. Chung, D.-G. Kim, and N. Dagli, "Reflection properties of coupled-ring reflectors," *J. Lightwave Tech.*, **24**, pp. 1865 (2006).

[15] D. Goldring, U. Levy, and D. Mendlovic, "Highly dispersive micro-ring resonator based on one dimensional photonic crystal waveguide design and analysis," *Opt. Exp.*, **15**, pp. 3156 (2007).

[16] T. Wang, Z. Zhang, F. Liu, Y. Tong, J. Wang, Y. Tian, M. Qiu, and Y. Su, "Modeling of quasi-grating sidewall corrugation in SOI microring add-drop filters," *Opt. Communications*, **282**, pp. 3464 (2009).

[17] R. Grover, "Indium phosphide based optical micro-ring resonators," Ph. D. dissertation, University of Maryland, College Park, MD, 2003 [Online]. Available: http://www.ece.umd.edu/research/microphotonics/

[18] J. Heebner, R. Grover, and T. Ibrahim, *Optical Microresonators: Theory, Fabrication, and Applications*, Springer, 2007.

[19] A. Yariv, "Universal relations for coupling of optical power between microresonators and dielectric waveguides," *Electron. Lett.*, **36**, pp. 321 (2000).

[20] L. A. Coldren and S. W. Corzine, *Diode Lasers and Photonic Integrated Circuits*, Wiley-Interscience, 1995.

[21] Y. M. Kang and L. L. Goddard, "Semi-analytic modeling of microring resonators with distributed Bragg reflectors," *Numerical Simulation of Optoelectronic Devices, 2009. NUSOD 2009. 9th International Conference on*, pp. 123 (2009).

[22] Y. M. Kang and L. L. Goddard, "A microring resonator with an integrated Bragg grating: a compact replacement for a sampled grating distributed Bragg reflector," *Opt. Quantum Electron.*, accepted (2010).

[23] Z. Zhang, M. Dainese, L. Wosinski, and M. Qiu, "Resonance-splitting and enhanced notch depth in SOI ring resonators with mutual mode coupling," *Opt. Exp.*, **16**, pp. 4621 (2008).

[24] V. Jayaraman, Z.-M. Chuang, and L. A. Coldren, "Theory, design, and performance of extended tuning range semiconductor lasers with sampled gratings," *IEEE J. Quantum Electron.*, **29**, pp. 1824 (1993).